

# 1 Spatial influence of fault-related stress perturbations in 2 northern Switzerland

3 Lalit Sai Aditya Reddy Velagala<sup>1,4</sup>, Oliver Heidbach<sup>1,2</sup>, Moritz Ziegler<sup>1,3</sup>, Karsten Reiter<sup>4</sup>, Mojtaba Rajabi<sup>5</sup>, Andreas Henk<sup>4</sup>, Silvio  
4 B. Giger<sup>6</sup>, Tobias Hergert<sup>7</sup>.

5 1 GFZ Helmholtz Centre for Geosciences, Telegrafenberg, 14473 Potsdam, Germany.

6 2 Institute for Applied Geosciences, Technische Universität Berlin, 10587 Berlin, Germany.

7 3 Professorship of Geothermal Technologies, Technical University Munich, 80333 Munich, Germany.

8 4 Institute of Applied Geosciences, Technische Universität Darmstadt, 64287 Darmstadt, Germany.

9 5 School of the Environment, The University of Queensland, QLD, 4072, Australia.

10 6 National Cooperative for the Disposal of Radioactive Waste, 5430 Wettingen, Switzerland.

11 7 Institute of Applied Geosciences, Karlsruhe Institute of Technology, 76131 Karlsruhe, Germany.

## 12 Abstract

13 The spatial influence of faults on the crustal stress field ~~remains-is~~ a topic of ~~ongoingactive~~ debate. ~~While it is well-documented that faults are often known to perturb because perturbations in~~ the stress field at a meter scale,   
14 ~~their lateral influence over a greater distances, from a few hundred meters to several kilometers, remains poorly understood. This knowledge gap largely results from the lateral resolution limit of stress data.~~ To address   
15 ~~this knowledge gap~~, we use a 3D geomechanical numerical model based on 3D seismic data from northern   
16 Switzerland. ~~The model is calibrated with 45 high-quality horizontal stress magnitude data obtained from micro-hydraulic fracturing (MHF) and sleeve re-opening (SR) tests conducted in two boreholes in the Zürich Nordost (ZNO) siting region, northern Switzerland. The 3D seismic and stress data were collected as a part of site characterization for a potential Deep Geological Repository (DGR) for radioactive waste.~~ This 3D geomechanical numerical model ~~with seven faults implemented as contact surfaces~~   
17 serves as the reference model in our study, ~~and includes seven faults, implemented as contact surfaces with Coulomb friction. The reference model~~ is then systematically compared to three fault-agnostic models, *i.e.*,   
18 ~~models without any implemented faults which share~~. ~~These fault agnostic models use identical rock properties, model and model input parameters~~ dimensions, ~~and calibration data with the reference model are calibrated with the same 45 horizontal stress magnitude dataset and have the same model extent~~, but differ in their   
19 ~~element resolution~~ discretization and mechanical properties' assignment procedure. ~~The results~~ Results show   
20 ~~that at distances of <1 km from faults, differences in maximum horizontal stress orientation between models range from 3°–6°, and horizontal stress magnitude differences are approximately 1–2 MPa. Beyond 1 km, these differences reduce to <1.5° and <0.5 MPa, respectively. These stress differences are significantly smaller than the calibration data uncertainties associated with the horizontal stress magnitude measurements at ZNO the ZNO siting region, which average to ±0.7 MPa and ±3.5 MPa for the minimum horizontal stress magnitude and ±3.5 MPa for the maximum horizontal stress magnitude, respectively, and ±11° for the maximum horizontal stress orientation.~~ An important implication of this lateral   
21 ~~quantification of fault influence on stress state of our results~~ is that, ~~under the specific geological, mechanical, and stress conditions observed at the ZNO siting region~~, explicit representation of faults may not be necessary in   
22 geomechanical models predicting the stress state of rock volumes located a kilometer or more from ~~major~~ active   
23 faults, ~~an important prerequisite for any DGR campaign. This is structural simplification substantially reduced our model setup time from 2 months to 2 days allows for faster model set-up and discretization, leading to a significant reduction in the set up phase and computational time by more than one order~~, without compromising   
24 the reliability of stress field predictions.

## 43 Short summary

44 We assess the ~~fault impact~~ on the stress field in northern Switzerland using 3D geomechanical   
45 models, calibrated with stress ~~data~~. We ~~see~~ that faults affect the stresses only locally, with negligible   
46 impact beyond 1 km, suggesting that faults may not be necessary ~~in~~ reservoir-scale models predicting stresses   
47 of undisturbed rock volumes, such as for a ~~deep~~ geological repository. Omitting them can substantially reduce   
48 model ~~set-up~~ time and computational cost without compromising prediction ~~reliability~~ accuracy.

## 49 1. Introduction

50 Characterizing the crustal stress field is essential for understanding both global and local tectonic deformation  
51 processes. On a large scale, it provides insights into plate tectonics (Richardson et al., 1979; Cloetingh and Wortel,  
52 1985; Rajabi et al., 2017b) and earthquake mechanics (Sibson, 1992; Sibson et al., 2011; Brodsky et al., 2020),  
53 while on a local scale, it plays a critical role in the safe planning of many subsurface applications, including  
54 ~~subsurface~~ oil and gas exploration and storage (Berard et al., 2008; Zoback, 2009; Fischer and Henk, 2013),  
55 geothermal exploration (Catalli et al., 2013; Schoenball et al., 2014; Azzola et al., 2019) and deep geological  
56 repositories for nuclear waste (Long and Ewing, 2004; Gens et al., 2009; Jo et al., 2019). The present day stress  
57 state also significantly impacts wellbore stability and trajectory optimization, reducing risks and improving drilling  
58 operations (Kingsborough et al., 1991; Henk, 2005; Rajabi et al., 2016). Moreover, knowledge of the regional and  
59 local stress field aids in assessing seismic hazards and understanding the potential ~~generation or~~ reactivation-~~or~~  
60 ~~generation~~ of faults (Zakharova and Goldberg, 2014; Seithel et al., 2019; Vadacca et al., 2021).

61 The stress state at a point is described by the Cauchy stress tensor, a symmetric second-order tensor with six  
62 independent components. This tensor can be transformed into ~~at the~~ principal stress system, where only three  
63 mutually perpendicular normal stresses, known as the principal stresses ( $S_1$  = maximum principal stress;  $S_2$  =  
64 intermediate principal stress, and  $S_3$  ~~is the~~ minimum principal stress), remain, and the shear stresses are zero.  
65 In reservoir geomechanics, where the target area is the upper crust, it is typically assumed that the principal  
66 stresses are the vertical stress ( $S_v$ ), the maximum horizontal stress ( $S_{Hmax}$ ), and ~~the~~ minimum horizontal stress  
67 ( $S_{Hmin}$ ). Based on this, the reduced stress tensor is ~~defined by established by four key parameters: the magnitudes~~ of  
68  $S_v$ ,  $S_{Hmax}$ , and  $S_{Hmin}$ , and the orientation of  $S_{Hmax}$  (Jaeger et al., 2007; Zoback, 2009).

69 The  $S_{Hmax}$  orientation is the most widely available, systematically documented, and freely accessible ~~characteristic~~  
70 ~~of the~~ reduced stress tensor ~~component~~, compiled in ~~a~~ publicly available database of the World Stress Map  
71 project (Heidbach et al., 2018; Heidbach et al., 2025a). Analyzing the patterns of the  $S_{Hmax}$  orientation shows  
72 consistent trends over hundreds of kilometers in intra-continental areas, primarily driven by first-order plate  
73 tectonic forces and second-order buoyancy forces (Zoback et al., 1989; Zoback, 1992; Rajabi et al., 2017b;  
74 Heidbach et al., 2018). At the same time, in some regions, significant rotations exceeding 30° are observed on  
75 spatial scales ranging from a few tens to a few hundreds of kilometers. It is hypothesized that these variations in  
76  $S_{Hmax}$  orientations, ~~among other reasons~~, arise from ~~mm third order sources, mainly the active~~ faults (Zoback et al.,  
77 1987; Yale, 2003; Heidbach et al., 2007; Tingay et al., 2009; Rajabi et al., 2017b).

78 A common approach to ~~understanding~~ the fault impact on the stress field is to visually interpret laterally  
79 scattered  $S_{Hmax}$  orientation data. This often leads to attributing the observed variability in  $S_{Hmax}$  orientation to the  
80 faults present within their respective study areas (Yale et al., 1994; Bell, 1996b; Yale, 2003; Aleksandrowski et  
81 al., 1992). While these studies are often convincing, they face two key issues: First, even in areas with relatively  
82 high data coverage, such as northern Switzerland (Heidbach et al., 2025a; Heidbach et al., 2025b), and the  
83 northern Bowen Basin (Rajabi et al., 2024; Heidbach et al., 2025a), ~~the usable publicly available data records and~~  
84 ~~their resolution are the data density is~~ fairly low, with, ~~on average, approximately about~~ one data record per 138  
85 km<sup>2</sup> lateral spatial distance, and one data record per 80 km<sup>2</sup> lateral spatial distance, respectively. Second,  
86 individual  $S_{Hmax}$  orientations ~~usually~~ have an average standard deviation of ±15° (A-Quality) to ±25° (C-Quality),  
87 as defined in the World Stress Map (Heidbach et al., 2025a). Together, these issues ~~do not allow make it difficult~~  
88 ~~for to attribute attributing~~ with confidence ~~the small perturbations in the stress rotations in the  $S_{Hmax}$  orientations~~  
89 to the faults, especially at spatial scales of 0.1–10 km.

90 Notable studies from regions with a comprehensive  $S_{Hmax}$  orientation dataset show that large-scale faulting does  
91 not necessarily result in abrupt ~~rotations in the~~  $S_{Hmax}$  orientation ~~rotations~~ over continental (>500 km) and  
92 regional scales (100–500 km). For instance, in eastern Australia, the  $S_{Hmax}$  orientation rotates smoothly, by up to  
93 50° over less than 100 km despite varying dip and strikes of the major fault systems, from northern Bowen Basin  
94 to southern Bowen and Surat basins (Brooke-Barnett et al., 2015; Tavener et al., 2017; Rajabi et al.,  
95 2024)(~~Brooke-Barnett et al., 2015; Rajabi et al., 2024~~) (Fig. 1aA–bB). However, in the adjacent Clarence-Moreton  
96 Basin, rotation of  $S_{Hmax}$  orientations is prominent and abrupt when viewed in ~~conjugation conjunction~~ with the  
97 faults (~~Rajabi et al., 2015; Rajabi et al., 2017b; Rajabi et al., 2017c~~) (~~Rajabi et al., 2017b; Rajabi et al., 2017c;~~  
98 ~~Tavener et al., 2017; Mukherjee et al., 2020~~) (Fig. 1aA–bB). Comparable conflicting trends have been reported

99 in other studies as well (Bell and Gough, 1979; Gough and Bell, 1982; Bell and Grasby, 2012), suggesting that the  
100 influence of fault systems on the rotation of  $S_{H\max}$  orientation ~~rotations~~ at continental and regional scales is not  
101 straightforward, and often not resolvable without ambiguity.

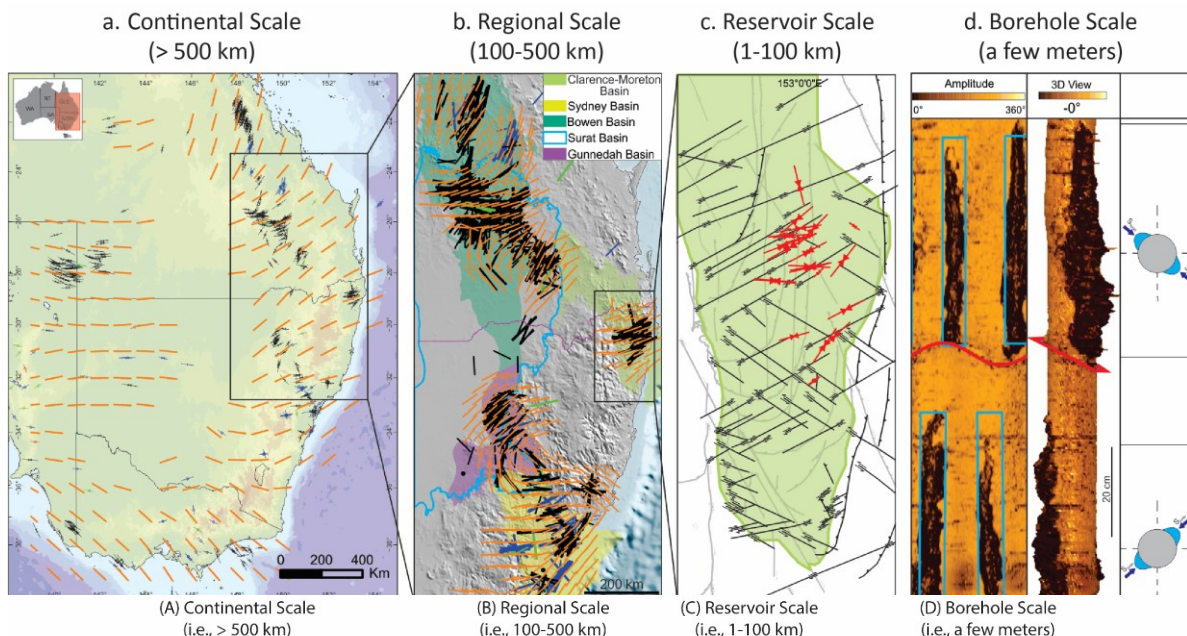
102 ~~The stress maps typically display an average of all the  $S_{H\max}$  orientation along the length of a borehole and does not capture potential changes in  $S_{H\max}$  orientation with depth due to interaction with the faults. At the borehole scale studies, distinct variations in  $S_{H\max}$  orientation have been observed vertically on a spatial scale of a few meters. For instance, Fig. 1d shows an image log of a borehole from the Clarence-Moreton Basin, where the  $S_{H\max}$  orientation abruptly changes by 90° when the borehole intersects a fault. This is also observed in the San Andreas Fault Observatory Drilling Borehole, where borehole breakouts (BO) and drilling-induced tensile fractures (DITF) indicate a change in  $S_{H\max}$  orientation from 25° ± 10° at 1000–1500 m (true vertical depth; t.v.d) to 70° ± 14° at 2050–2200 m (t.v.d) (Chéry et al., 2004; Hickman and Zoback, 2004; Boness and Zoback, 2006; Zoback et al., 2011). Also, in the KTB drilling program,  $S_{H\max}$  orientation along the borehole remained consistent with the regional tectonic-induced patterns except at a depth of 7200 m (t.v.d), where a major fault zone caused a localized reorientation by about 60°, confined to only a few meters above and below the fault (Brudy et al., 1993; Barton and Zoback, 1994; Brudy et al., 1997).~~

114 ~~Similar localized stress reorientations near fault zones and pre-existing fractures have been reported in other boreholes (Ando, 2001; Tsukahara et al., 2001; Lin et al., 2010; Nie et al., 2013; Cui et al., 2014; Jo et al., 2019; Massiot et al., 2019; Rajabi et al., 2022; Li et al., 2025). However, borehole-scale studies are generally conducted in vertical wells and do not capture the potential lateral variations in stress caused by faults. Therefore, it remains unclear whether these localized findings can be directly be extrapolated to explain stress field variations at larger spatial scales away from the fault zone. This leads to a significant knowledge gap regarding fault's influence on stress field variations at the reservoir scale (Fig. 1c), a scale particularly important for many subsurface applications.~~

122 ~~The major challenge for studies focusing on stress field predictions at reservoir spatial scales is the scarcity of stress magnitude measurements, which makes geomechanical numerical modeling the most effective and often the only viable approach for predicting the variations in the stress field at this scale is geomechanical numerical modelling. Over the past few decades, 2D and 3D geomechanical numerical models have been developed for this purpose (Henk, 2009, 2020; Treffeisen and Henk, 2020). These can broadly be grouped into three categories: 1) site-specific models without fault representation (Lecampion and Lei, 2010; Rajabi et al., 2017c; Ahlers et al., 2021), 2) site-specific models that include faults but are not explicitly focused on assessing influence of faults on the predicted stress (Reiter and Heidbach, 2014; Hergert et al., 2015; Bérard and Desroches, 2021) and 3) generic models that explicitly investigates the impact of faults (Homberg et al., 1997; Su and Stephansson, 1999; Reiter et al., 2024; Ziegler et al., 2024). While models without faults are understandably not suitable for evaluating fault-related stress perturbations, the latter two categories often have limited or no access to reliable in situ stress magnitude data. This hinders their ability to reliably represent fault-related stress variations in real-world scenarios, as seen in studies by Ziegler et al. (2016) and Hergert and Heidbach (2011). The necessity to include faults in the models also could not be meaningfully addressed, especially if the model aims to predict the stress field within an intact and undisturbed rock volume, located away from active faults.~~

137

138



139

140 Figure 1:  $S_{\text{Max}}$  orientation stress maps from eastern Australia at a**A**) Continental Sscale; b**B**) Regional Sscale; c**C**) Reservoir Sscale, and d**D**) Borehole Sscale. On continental and regional scales, visual observations suggest that faults may have differing influences, as seen in the uniform stress orientation (orange lines) across eastern Australia despite the presence of faults. However, on a borehole scale, faults can cause local perturbations, evident in the shift of borehole breakout orientations (blue box), which reflect stress variations across the fault (red line). While research primarily focuses on these three scales, studies examining reservoir scales are scarce due to lack of reliable stress magnitude data, making it challenging to quantify the spatial influence of faults on the reduced stress tensor components (Image adopted from Rajabi et al. (2017c)).

147 In our study, we use 45 reliable and robust stress magnitudes data records, obtained from two deep boreholes, Trüllikon (TRU1-1) and Marthalen (MAR1-1) (Marthalen), using microhydraulic fracturing (MHF) and dry sleeve re-opening (SR) test (Desroches et al., 2021a; Desroches et al., 2021b; Desroches et al., 2023) to calibrate 3D 148 geomechanical numerical models of the Zürich Nordost (ZNO) siting region, northern Switzerland (Fig. 2). The 149 data records were collected during a comprehensive 3D seismic and drilling campaign to support site selection 150 for a deep geological repository (DGR) of radioactive waste (Nagra, 2024c, a). The stress magnitudes presented 151 in this study are the total stresses, and any reference to the stress magnitudes must be taken as such. Four 152 variants of the 3D geomechanical numerical model of the siting region, each with lateral dimensions of 14.7 km 153  $\times$  14.8 km, and a vertical depth of 2.5 km (below sea level; b.s.l.)<sub>1</sub> are used within this study. All models use 154 identical mechanical properties and the same representation of geomechanically relevant subsurface units. One 155 of the models includes seven contact surfaces with an assigned Coulomb friction coefficient representing 156 faults, and serves as the reference model (REF model) (Nagra, 2024d, c), while the other three models are fault-agnostic, 157 i.e., faults are excluded from the model. By systematically comparing the predicted stress fields across all the 158 models, we illustrate the observed perturbations in the stress field with respect to the reference model and 159 quantify the spatial extent of the stress perturbations caused by faults. 160

162 2. 3D ~~g~~Geomechanical ~~N~~umerical ~~m~~odel with ~~F~~ault ~~r~~espresentation

163 2.1 Geological ~~b~~ackground and ~~m~~odel ~~g~~eometry

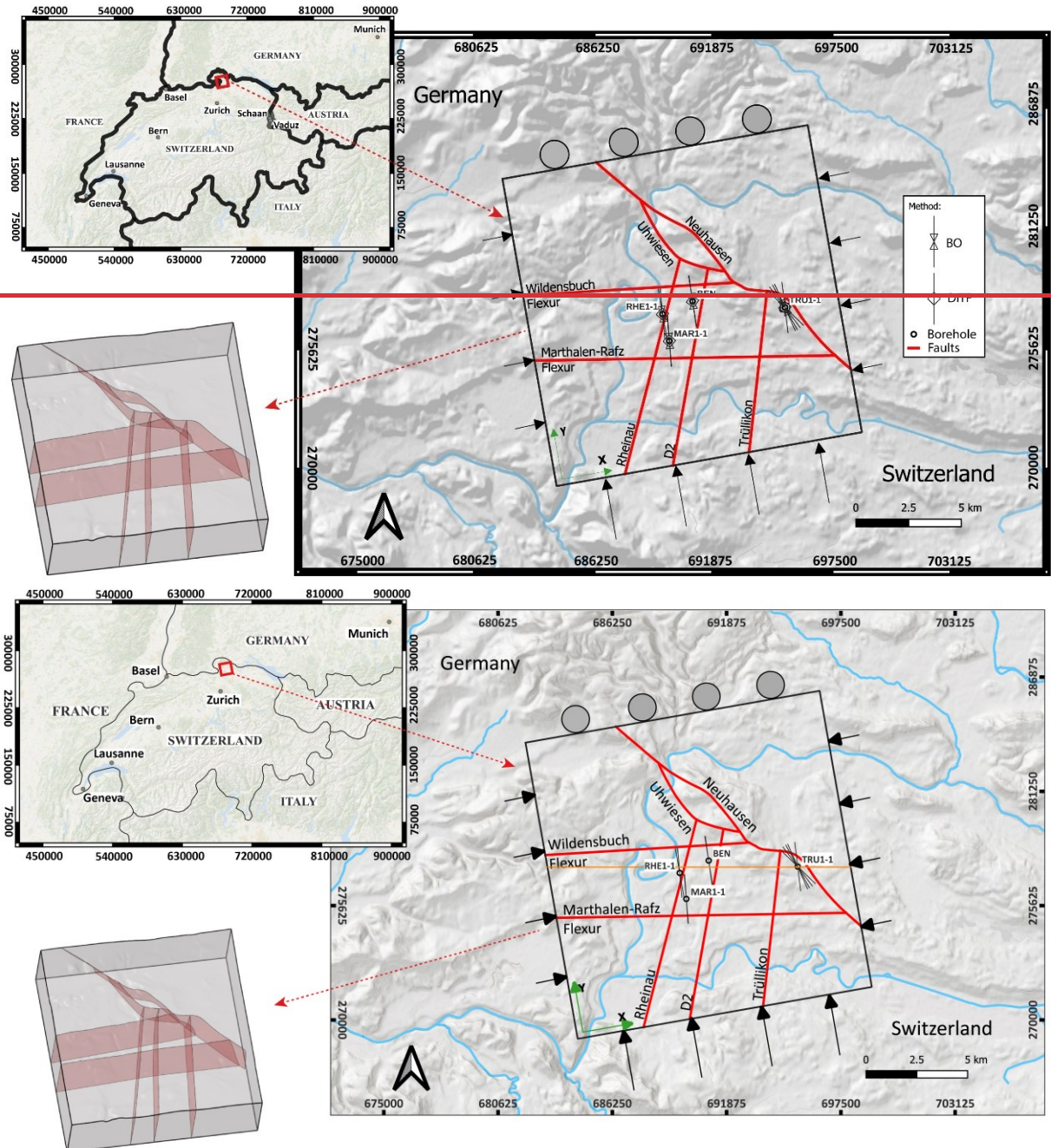
164 The ZNO study ~~area~~region is located in the northern Alpine Foreland of northern Switzerland, approximately 30  
165 km NNE of Zurich (Fig. 2). It is close to the ~~Black Forest~~ in SW ~~of~~ Germany, where pre-Mesozoic basement rocks  
166 locally outcrop (Nagra, 1984, 2002a). The geological evolution of this region was influenced by the development  
167 of a WSW–ENE striking Permo-Carboniferous basin (Gorin et al., 1993; Mccann et al., 2006; Nagra, 2014), formed  
168 in response to the Variscan orogeny and subsequent post-orogenic transtensional processes (Nagra, 1991;  
169 Marchant et al., 2005).

170 During the Mesozoic, a sequence of sedimentary successions was deposited on ~~the~~ top of the Variscan basement.  
171 This depositional process was prominent, especially from the Early to Middle Jurassic due to a combination of  
172 regional tectonic subsidence and sea level changes (Coward and Dietrich, 1989; Nagra, 2024c). The sedimentary  
173 rocks were originally deposited directly on the ocean floor as a result of the landmass corresponding to the  
174 present day ~~n~~Northern Switzerland being submerged in a broad and shallow epicontinental marine setting  
175 (Jordan, 2008; Reisdorf et al., 2011). The Opalinus Clay formation, deposited during the Jurassic Period of the  
176 Mesozoic Era, is of particular importance as it has been selected as the host rock for Switzerland's DGR. Factors  
177 contributing to the effectiveness of Opalinus Clay as a long-term geological barrier are its favorable mineralogy  
178 and associated low permeability, and good sorption and self-sealing properties (Nagra, 2001, 2002b, 2008).

179 At ~~the~~ late Cretaceous and onset of the Cenozoic, the Alpine orogeny, formed by the collision of Adriatic and  
180 Eurasian tectonic plates, led to a significant tectonic activity in the European northern Alpine Foreland (Illies,  
181 1972; Schmid et al., 1996; Schmid et al., 1997; Cloetingh et al., 2006). This resulted in the formation of basement-  
182 rooted, NNE-striking normal faults, forming the Upper Rhine Valley in combination with the uplift of the Black  
183 Forest and Vosges Mountain Massifs. The formation of the flexural Molasse Basin during the Late Oligocene to  
184 Early Miocene is a result of ~~the~~ downbending of the European plate, in response to the orogenic loading of the  
185 Alps, and caused a gentle ~~north-south~~dip from north to south in the Mesozoic strata (Sinclair and Allen, 1992;  
186 Kempf and Adrian, 2004; Sommaruga et al., 2012). In our study ~~area~~region, the Mesozoic strata gently dips SSE  
187 (Fig. 3). In the Late Miocene, continued Alpine deformation propagated into the ~~n~~Northern Foreland, resulting  
188 in the formation of the Jura Mountains and their associated fold-and-thrust belt, primarily further to the west,  
189 and reactivating the pre-existing basement structures (Diebold and Noack, 1997; Burkhard and Sommaruga,  
190 1998; Laubscher, 2010). These tectonic processes, along with the glacial-interglacial cycles during ~~the~~ Pleistocene  
191 (Fiebig and Preusser, 2008; Preusser et al., 2011), have established the present day geological and stratigraphic  
192 setting in the region.

193 The reference model (REF ~~m~~odel) is rectangular, spanning 14.7 km E-W  $\times$  14.8 km N-S laterally, and extending  
194 to a depth of 2.5 km below sea level (b.s.l). The upper boundary is defined by the local topography. In the siting  
195 ~~area~~region,  $S_{H\max}$  orientation is  $170^\circ \pm 11^\circ$  according to the BO and DITF observations from the boreholes, in  
196 agreement with the regional trend (Nagra, 2013; Heidbach et al., 2025b). To align the model geometry with the  
197  $S_{H\max}$  orientation, the entire model domain is rotated by  $10^\circ$  counterclockwise from geographic north, such that  
198 its sides are parallel and perpendicular to the mean  $S_{H\max}$  orientation (Fig. 2).

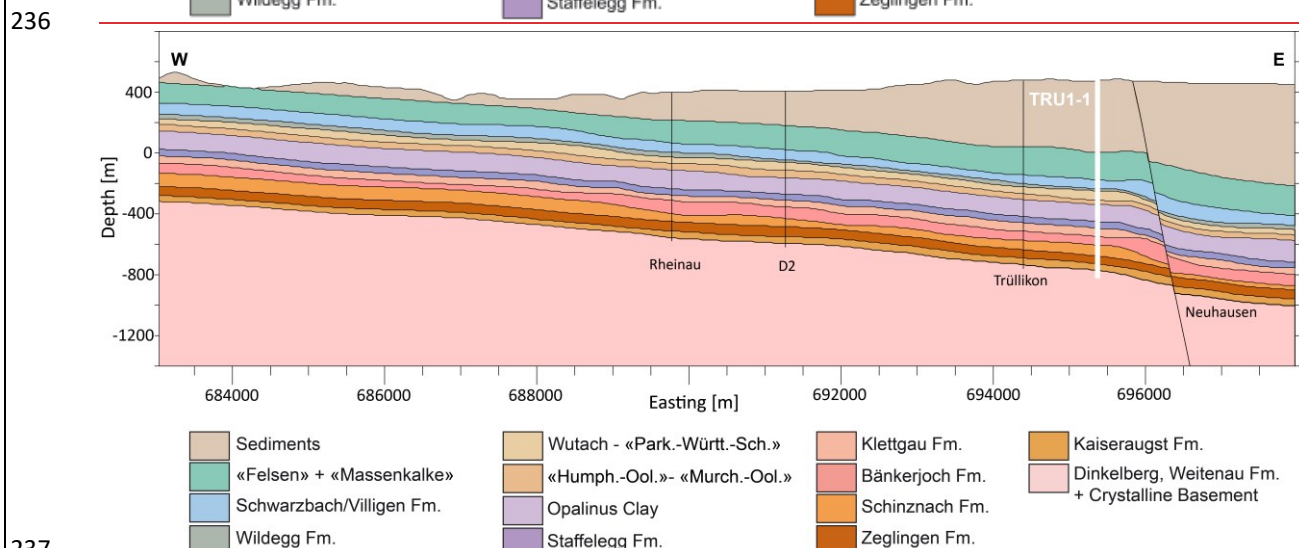
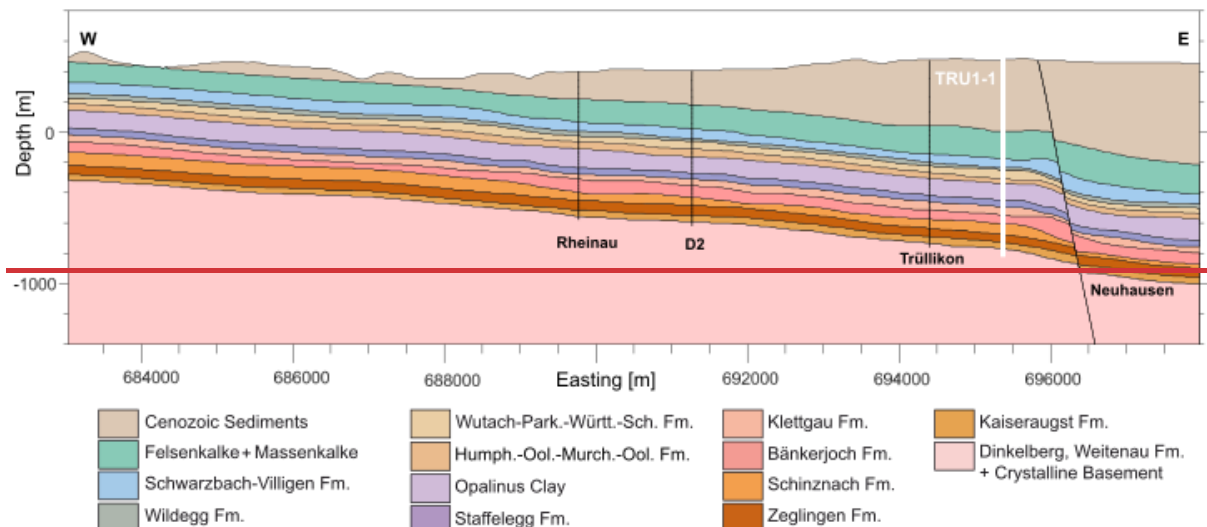
199 The present day geomechanically relevant layers were constructed using SKUA-GOCAD v19 software. Successive  
200 lithologies with comparable mechanical properties were combined (Table 1), eventually leading to 14  
201 geomechanically different units in the REF model (Fig. 3). A total of seven faults and flexures, named Neuhausen,  
202 Uhwiesen, Wildensbuch, Marthalen-Rafz Flexure, Rheinau, D2, and Trüllikon, were implemented in the model  
203 (Fig. 2). These structures are modeled as contact surfaces, weakly interpreted from the regional 3D seismic  
204 sections, and are highly simplified for ease of implementation in the model. Here, simplification means merging  
205 much smaller segments interpreted on 3D seismics into larger, continuous fault planes to represent what is, in  
206 reality, a volumetric fault zone structure (Nagra, 2024a) (Fig. 2, 3).



208  
209 Figure 2: ~~The~~ geographical location and the model boundaries of the ZNO siting region. The red lines within the model  
210 extents represent the surface trace of the faults and flexures, interpreted from the seismic sections of the siting region and  
211 extrapolated to the surface. The location of the boreholes Trüllikon (TRU1-1), Benken (BEN), ~~MAR1-1~~ Marthalen (MAR1-  
212 ~~1~~ Marthalen), and Rheinau (RHE1-1) ~~are~~ is shown, along with the  $S_{H\max}$  orientation data records from each borehole (black  
213 lines with the centre at the boreholes). The light brown line is the surface trace of a W-E cross-section, along which all the  
214 results in our study are plotted. The model is rotated by 10° anticlockwise according to the regional  $S_{H\max}$  orientation values.  
215 The black arrows on the sides of the model are the displacement boundary conditions /compression applied on the model  
216 boundaries, where the length of the arrows is proportional to the magnitude of the displacement applied. The grey circles  
217 on in the north of the model indicate that the displacements are constrained perpendicular to this boundary. The co-ordinate  
218 reference system used is CH1903 ~~AV03~~. The insert at the bottom left is the 3D view of the faults (~~light-red~~ red) within the  
219 model geometry (grey box).  
220

221 The present day geomechanically relevant layers were constructed using SKUA-GOCAD v19 software. Successive  
222 lithologies with comparable mechanical properties were combined (Table 1). Eventually, the REF model consists  
223 of 14 geomechanically different units (Fig. 3). A total of seven faults and flexures, named Neuhausen, Uhwiesen,  
224 Wildensbuch, Marthalen-Rafz Flexure, Rheinau, D2, and Trüllikon, were implemented in the model (Fig. 2). These  
225 structures are modeled as contact surfaces, weakly interpreted from the regional 3D seismic sections, and are  
226 highly simplified for ease of implementation in the model. Here, simplification means merging much smaller

227 segments on 3D seismics into larger, continuous fault planes (Nagra, 2024a) (Fig. 2, 3). Among the faults and  
 228 flexures, Both Neuhausen and Uhwiesen faults dip at 60° toward the northeast, while the others are vertical.  
 229 Neuhausen is the only fault that has displays a stratigraphic offset, with a vertical displacement of approximately  
 230 50 m at the base of the Mesozoic units that decreases towards the surface (Nagra, 2002a, 2008, 2024d). The  
 231 Marthalen-Rafz Flexur and Wildensbuch Flexur are monoclines that dominate the overlying Mesozoic strata in  
 232 the siting region through a step-like bending rather than a discrete break in an otherwise dipping strata  
 233 (Madritsch et al., 2024; Nagra, 2024c). Other than the Neuhausen fault, the remaining faults and flexures show  
 234 no clear displacement but are included in the model as they represent the first-order geological structures of the  
 235 ZNO siting region. (Madritsch et al., 2024; Nagra, 2024 #350)1



236  
 237  
 238 Figure 3: W-E cross-section of the geomechanical units passing through the Trüllikon borehole (Bold white line, TRU1-1) and  
 239 a constant northing = 277548 m within the REF model domain. The depth is referenced to the sea level. The model includes  
 240 14 geomechanical units that exhibit a gentle W-E dip in this cross-section. No stratigraphic offset is observed across the faults,  
 241 except the Neuhausen fault, which displays a vertical stratigraphic offset of approximately 50 m. Vertical exaggeration by a  
 242 factor of 2.5 is applied to enhance the visibility of thin layers, such as the Wildegg Formation. The respective mechanical  
 243 properties are shown in Table 1. Only depths down to -1400 m (b.s.l) are shown for clarity, although the REF model extends  
 244 to -2500 m (b.s.l). The co-ordinate reference system used is CH1903/LV03.

245 2.2 Reference Model (REF model) setup

246 2.2.1 Model Assumptions

247 The primary objective of the REF model is to reliably predict the present day in-situ stress state within the ZNO  
248 siting region, ~~using the rock properties and stress magnitude data obtained from deep borehole drilling.~~ To  
249 achieve this, two key simplifying assumptions are made. First, transient effects such as time-dependent tectonic  
250 deformation, or human-induced changes ~~can be are~~ neglected while considering only the stress contributions  
251 from the gravitational and tectonic forces. Since the model focuses on static stress field prediction, the rock  
252 volume is assumed ~~to not~~not to undergo any transient deformation. Second, linear isotropic elasticity is assumed  
253 in the geomechanical units within the rock volume. This assumption simplifies the ~~required~~ material parameters  
254 needed to explain the behavior of the rock under stress to just the Young's modulus which characterizes the  
255 elastic stiffness of the rock (E), Poisson's ratio which describes the lateral strain response (v), and density ( $\rho$ ) of  
256 each geomechanical unit. Throughout this work, we will refer to Young's modulus as stiffness and the contrast  
257 in Young's modulus as stiffness contrast. The equilibrium condition between the gravitational and the tectonic  
258 forces is governed by a second-order partial differential equation (PDE), with displacement as the field variable  
259 (Jaeger et al., 2007). Since this PDE cannot be solved analytically, a numerical solution ~~approach~~ is needed.  
260 Therefore and for this, we use the Finite Element Method (FEM). FEM allows the use of unstructured meshes to  
261 represent the model volume, which is particularly useful when modeling complex geological features, and  
262 variations in material properties (Mao, 2005; Henk, 2009).

263 Although several studies have shown that the stress state can be dominated by inelastic deformations once the  
264 elastic limits of the geomechanical units are exceeded (Smart et al., 2012; Pijnenburg et al., 2019; Yan et al.,  
265 2025), linear elasticity remains an appropriate first-order approximation for predicting the present day stress  
266 state in the ZNO siting region. This assumption is supported by several geological factors (Nagra, 2024d, c). The  
267 tectonic strain rates in northern Switzerland are extremely low, in the order of 1-3 m/Myr/km, and the region is  
268 tectonically stable, with no significant deformation observed since the Miocene. More importantly, the observed  
269 differential stresses ( $S_1-S_3$ ) within the geomechanical units range between 0.5–13 MPa, which are significantly  
270 lower than their measured uniaxial compressive strength limits of 33–180 MPa. Because the differential stresses  
271 in the geomechanical units are far below their peak strength, plastic deformation is not expected under the  
272 current stress state.

## 274 2.2.2 Model ~~d~~iscretization

275 The model setup follows a standard series of steps, previously used in other regional geomechanical studies  
276 (Buchmann and Connolly, 2007; Reiter and Heidbach, 2014; Hergert et al., 2015; Ziegler et al., 2016; Rajabi et al.,  
277 2017a). The model volume is discretized into 3D elements, collectively referred to as a mesh. The 3D element  
278 resolution plays a significant role in capturing predicted stress variations, where smaller elements capture a  
279 higher spatial resolution but at increased computational cost (Ahlers et al., 2021; Ahlers et al., 2022). To ensure  
280 a reasonably accurate representation of each geomechanical unit, a minimum of three finite elements ~~are is~~ used  
281 in the vertical direction. Accordingly, the top 13 geomechanical units, which are relatively thin (Fig. 3), are  
282 discretized with smaller element sizes vertically, whereas the deeper and thicker Basement unit is represented  
283 with larger element sizes in the vertical direction. A total of 1,923,139 ~~finite-tetrahedral and hexahedral finite~~  
284 elements are used, providing a high-resolution representation of the geomechanical units, with model  
285 resolutions varying from 100–150 m laterally and 5–20 m vertically. We use first-order elements in this ~~study, study, with linear shape functions, and the~~ and the discretization is done using Altair HyperMesh 2023.1 software  
286 package.

## 288 2.2.3 Mechanical ~~r~~ock properties and ~~f~~Fault properties.

289 Geological units, with similar mechanical properties, are grouped into the same geomechanical unit for simplicity.  
290 Each element in the mesh is assigned mechanical properties based on the corresponding geomechanical unit.  
291 The mechanical properties E [GPa], v [-], and  $\rho$  [kg/m<sup>3</sup>], used in the models are derived from ~~petrophysical logs~~  
292 ~~and from uniaxial and triaxial compression tests core tests performed on the core samples and petrophysical logs~~  
293 obtained from the TRU1-1 and MAR1-1 boreholes (Nagra, 2024c, b). From the ~~range distribution~~ of values for  
294 each geomechanical unit, the median values (P50) are used for the model, summarized in Table 1. Geological

295 faults are implemented as contact surfaces that can slip under mechanical loading as a structural response to  
 296 stress conditions, depending on their frictional properties. In the REF model, contact surfaces are assigned a  
 297 friction coefficient of 1 and a zero cohesion, values chosen to best represent the fault properties in the region  
 298 (Nagra, 2024c).

299  
 300

301 Table 1: Different geological formations with respective mechanical properties. The abbreviations are used solely to indicate  
 302 the respective formations in the figures of this paper. Geological formations with similar geomechanical properties are  
 303 aggregated together in the 3D geomechanical numerical models and are referred to as geomechanical units throughout the  
 304 paper. Throughout the rest of this paper, the respective units can also be matched with the corresponding colors shown in  
 305 Fig. 3 and to-with the abbreviations given here(Nagra, 2024c, b). Detailed information on the lithology is given in (Nagra,

306 2024c, b).Nagra (2024c)

System	Group	Formation	Lithology	Abbreviation used	$\rho$ [kg/m <sup>3</sup> ]	$\nu$ [-]	E [GPa]
Quaternary, Paleogene, and Neogene		Cenozoic Sediments	<u>Sandstone</u> <u>(calc.)</u>	CeSe	2350	0.30	15
Jurassic	Malm	«Felsenkalke» + «Massenkalk»	<u>Limestone</u>	MaFeMa	2685	0.18	31
		Schwarzbach-Villigen Fm.	<u>Limestone</u> <u>(argill.)</u>	MaScVi	2685	0.20	40
		Wildegg Fm.	<u>Limestone</u>	MaWi	2610	0.26	18
	Dogger	Wutach Fm.	<u>Calc. marl</u>	DoWuVaPa	2530	0.32	13
		Variansmergel Fm.	<u>Silty marl</u>				
		«Parkinsoni-Wütembergica-Sch. »	<u>Silty marl</u>	DoHuWeMu	2540	0.28	14
		«Humphriesoolith Fm. »	<u>Silty marl</u>				
		Wedelsandstein Fm.	<u>Silty marl</u>				
		«Murchisonae-Oolith Fm.»	<u>Silty marl</u>				
		Opalinus Clay Fm.	<u>Silty claystone</u>	DoOp	2520	0.37	11
	Lias	Staffelegg Fm.	<u>Argill. marl</u>	LiSt	2540	0.26	18
Triassic	Keuper	Klettgau Fm.	<u>Dol. Marl</u>	KeKl	2570	0.23	17
		Bänkerjoch Fm.	<u>Anhydrite</u>	KeBä	2700	0.22	23
		Schinznach Fm.	<u>Dolostone</u> , <u>Limestone</u>	MuSc	2710	0.24	32
	Muschelkalk	Zeglingen Fm.	<u>Anhydrite</u>	MuZe	2840	0.19	36
		Kaiseraugst Fm.	<u>Argill.</u> <u>Marl</u>	MuKa	2620	0.30	23
		Bundsandstein	Dinkelberg Fm.	<u>Sandstone</u>	DiWeCr	2540	0.27
Permian	Rotliegend	Weitenau Fm.	<u>Argill.</u> <u>Sandstone</u>				
	Crustalline Basement	Crustalline basement.	<u>Crustalline</u> <u>basement</u>				

307

## 308 2.2.4 Model cCalibration

309 The present day stress state is computed by applying vertical loading simulating the gravitational forces and  
 310 lateral displacement boundary conditions to simulate the tectonic loading from the geological history. These  
 311 boundary conditions are chosen so that the modeled stresses best fit to-the measured horizontal stress  
 312 magnitude data, a process known as model calibration (Reiter and Heidbach, 2014; Ziegler and Heidbach, 2020).

313 The horizontal stress magnitude data are originally determined as ranges but the mean of these ranges was used  
314 for the model calibration. In total, we have 30  $S_{H\min}$  and 15  $S_{H\max}$  magnitudes (Fig. 5). The  $S_{H\min}$  magnitude ranges  
315 (Fig. 5: red bars) are derived from the micro-hydraulic fracturing (MHF) tests and dry sleeve reopening (SR) tests  
316 (Desroches et al., 2021a; Desroches et al., 2021b; Desroches et al., 2023; Nagra, 2024d) provide the basis to  
317 bracket the ranges for the  $S_{H\max}$  magnitudes (Fig. 5: blue bars). However, the mean of these ranges was used for  
318 the model calibration.

319 The model is calibrated with 30  $S_{H\min}$  and 15  $S_{H\max}$  magnitudes (Fig. 5). The model calibration is done using the  
320 PyFast Calibration tool (Ziegler and Heidbach, 2021), which uses a linear regression-based algorithm to compute  
321 the best-fit lateral displacement boundary conditions by minimizing the differences between the modeled and  
322 measured horizontal stress magnitudes. The resulting best fit for the boundary conditions of the model volume  
323 was found to be a To achieve the best fit of the boundary conditions, a total shortening total\_perpendicular  
324 displacement of 0.8822 m is applied in the east-west east-west direction, and 4.2 m in the north-south direction,  
325 both shortening the model volume, while the northern boundary remains fixed (Fig. 2). Displacements parallel  
326 to the boundaries are permitted on all lateral faces of the model. At the base, vertical displacement is constrained  
327 to zero, while horizontal displacement is permitted; the model top remains fully unconstrained. The numerical  
328 solution is computed using the Simulia Abaqus V2021 finite element solver. The results are analyzed using  
329 Tecplot 360 EX 2023 R2 along with the Geostress V2.0 add-on library (Stromeyer et al., 2020).

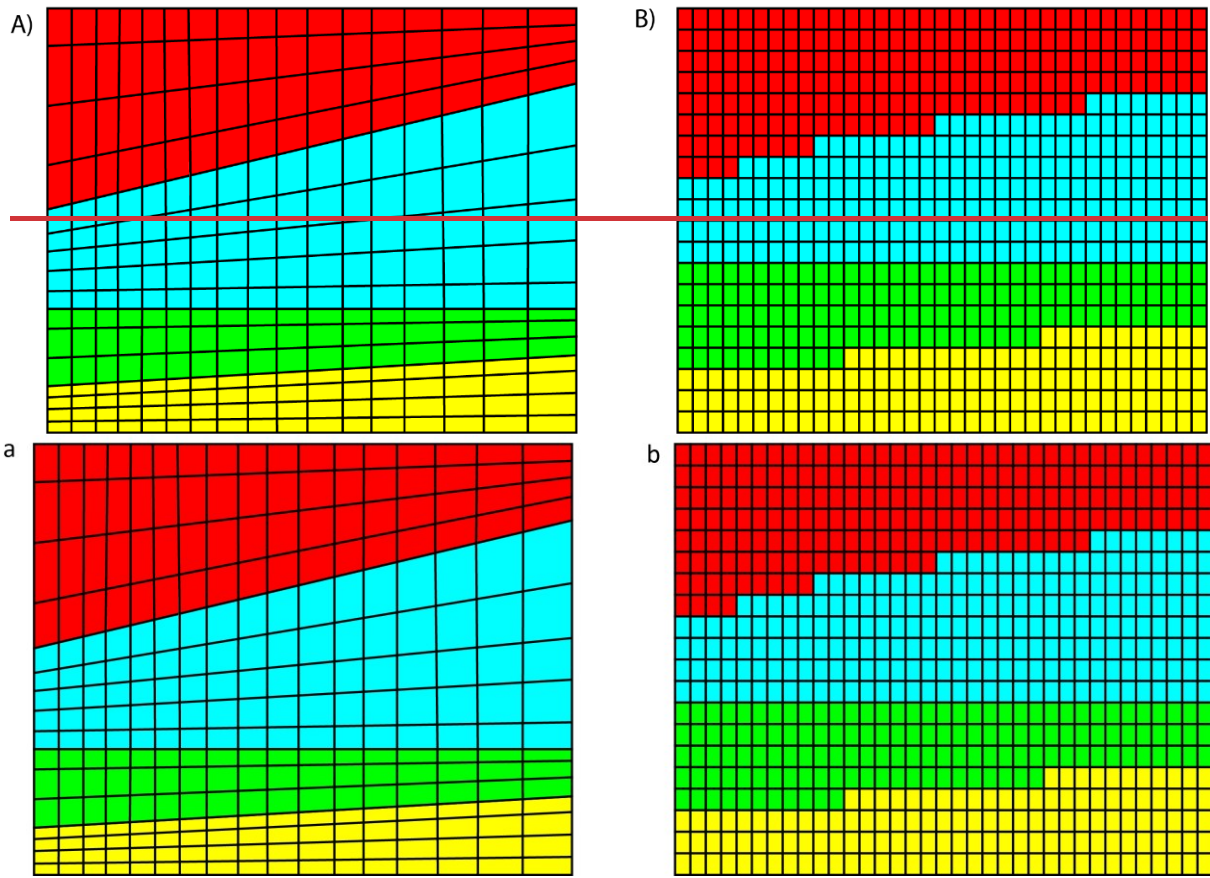
### 332 3. Model set-up of 3D gGeomechanical Annumerical Mmodels without 333 fFault Rrepresentation

#### 334 3.1 Model discretization strategies

335 Removing the fault implementation from the 3D models allows us to use different model discretization  
336 strategies, which in turn significantly accelerates the model setup and stress prediction workflow. Using two  
337 different discretization strategies, we developed three additional fault-agnostic 3D geomechanical numerical  
338 models. The reference model and the three fault-agnostic models are then compared to quantify the spatial  
339 influence of faults on the far-field stress state. In our study, the time required to build a model was reduced from  
340 approximately two months for the reference model, the model that includes contact surfaces, to just two days  
341 for the fault-agnostic models. Two different model discretization strategies were used to set up three additional  
342 fault agnostic 3D geomechanical numerical models.

343 The standard procedure discretizes each geomechanical unit individually using the definition of its top and  
344 bottom interface surfaces, and later connected by matching the nodes along the common interfaces. Each  
345 element of the unit is assigned to the appropriate mechanical properties (Fig. 4aA) directly from the stratigraphic  
346 definition. While this approach results in a smooth unit boundary, it requires substantial manual effort and is  
347 particularly time-consuming when working with models containing many geomechanical units.

348 In order to simplify the setup and discretization procedure of the fault-agnostic models, we use ApplePy  
349 (Automatic Partitioning Preventing Lengthy Manual Element Assignment), a Python-based tool that automates  
350 the discretization and element property assignment process (Ziegler et al., 2020). The entire model volume is  
351 discretized in a single step first as a largely homogeneous mesh, ignoring both lithological interfaces and fault  
352 structures. ApplePy uses the depth values of the stratigraphic boundaries to decide which element belongs to  
353 which lithological unit/geomechanical unit (Fig. 4Bb). Although this approach introduces step-like transitions at  
354 unit boundaries which looks optically unrealistic, it significantly reduces manual the meshing time, especially for  
355 large or complex models, like the REF model without compromising the stress prediction capability of the final  
356 3D geomechanical numerical models, as discussed in Sect. 4.



359 Figure 4: ~~A conceptual visual comparison of **aA**) the standard procedure and **Bb**) the ApplePy procedure for discretization~~  
 360 and mechanical property assignment to geomechanical units. The four colors represent distinct geomechanical units, each  
 361 with unique lithologies and mechanical properties. ~~In the standard procedure, each geomechanical unit is discretized~~  
 362 ~~individually and later connected to each other by matching the nodes along the common interfaces. The resulting~~  
 363 ~~geomechanical units' interfaces are smoother. The ApplePy procedure is significantly faster by approximately an order. Here,~~  
 364 ~~the whole model volume is discretized in a single step ignoring the interfaces. Due to the working principle of ApplePy, a step-~~  
 365 ~~like transitions at unit boundaries are observed.~~

### 3.2 Model Realizations and Configurations

368 ~~Building on the discretization strategies described in Sect. 3.1, three fault-agnostic 3D geomechanical numerical~~  
 369 ~~model realizations were developed.~~ The three fault-agnostic 3D geomechanical numerical models follow the  
 370 general model workflow of the REF model, i.e., the model parameterization and calibration are the same (Sect.  
 371 2.2), along with ~~the similar same model extents (Sect. 2.1). They are calibrated to the same dataset of 45~~  
 372 ~~horizontal stress magnitude measurements used for calibrating the REF model.~~ The only differences lie in the  
 373 model discretization strategies (Sect. 3.1) and ~~finite element~~ resolutions. Out of these three models, one is set  
 374 up using the standard procedure, and two are set up using the ApplePy procedure. Table 2 presents the technical  
 375 details on the number of elements and spatial resolution of each model used, along with the corresponding best-  
 376 fit displacement boundary conditions obtained after applying FAST Calibration tool. The brief description of the  
 377 three ~~fault-agnostic models without faults structures models is are~~:

- 378 • REF-NF ~~m~~Model: ~~REF-NF model is directly derived directly~~ from the REF model ~~with~~, maintaining  
 379 identical geometry, ~~mesh~~ and mechanical property assignments ~~but~~. ~~The only difference between this~~  
 380 ~~model and the REF model is that with~~ faults ~~removed are omitted~~. Contact surfaces are eliminated, and  
 381 ~~opposing nodes are equivalenced, except for the Neuhausen Fault, where a 50 m lithological offset~~  
 382 ~~prevents node equivalencing. In this case, slip is prevented by assigning an artificially high friction~~  
 383 ~~coefficient of 50~~  
 384 ~~This means for the six faults except the Neuhausen Fault that the contact surfaces are~~  
 385 ~~eliminated and double nodes on opposite sides of the former faults are equivalenced. For the~~  
~~Neuhausen Fault, this procedure is not possible due to the lithological vertical 50 m offset which is~~

represented in the mesh. To prevent slip along this surface, the fault's friction coefficient is artificially increased to 50.

- AP ~~m~~odel: ~~Maintains The AP model maintains~~ the same extents and mechanical properties as the REF and REF-NF models but uses ~~ApplePy a modified discretization, not tracking geological interfaces. for~~ ~~Property assignment to the elements is done using the ApplePy tool.~~ It does not incorporate faults, ~~eliminating the need for contact surfaces within the model framework~~ and has approximately 50% more elements than the REF and REF-NF models.
- AP-H model: ~~A~~ The AP-H model is a higher resolution version of the AP model, with twice the number of elements. All the other features of the model are the same as the AP model.

**Table 2: Summary of technical specifications for all model realizations used in this study. Reported vertical resolutions refer only to the Mesozoic units and are approximate for the ApplePy models due to depth-dependent variation. Minor differences in displacement boundary conditions reflect the presence of contact surfaces in the reference model, which allow elastic energy dissipation that is absent in the fault-agnostic models.** Summary of technical specifications for all model realizations used in this study. To ensure adequate numerical representation in the ApplePy models (AP and AP-H models), each geomechanical unit layer is modeled with at least three elements vertically, with a higher resolution allocated to the Mesozoic and Cenozoic units of interest compared to the basement. The boundary conditions are compressional in nature. The REF-NF, AP, and AP-H models have no fault representation. The listed vertical resolution values apply only to the Mesozoic units, as these are the target for planning the DGR facility. Vertical resolution values for ApplePy models are approximate, as they vary by geomechanical unit with depth.

Model Realization	Discretization procedure	Number of Elements	Vertical Resolution of the mesozoic Elements [m]	Lateral Resolution [m]	Displacement boundary conditions	
					North-South shortening [m]	East-West shortening [m]
REF model	Standard procedure	1,923,139	5-20	100-150	4.1	0.82
REF-NF model		1,923,139	5-20	100-150	4.2	0.90
AP model	ApplePy procedure	2,826,240	~7 (non-basement units)	80-110	4.23	0.93
AP-H model		5,974,150	~4 (non-basement units)	60-80	4.25	0.90

## 4. Results

#### 4.1 ~~1D results of the horizontal stress~~Stress magnitudes along ~~the~~ borehole trajectories

The resulting predicted horizontal-stress magnitudes from all the model realizations are presented together with the measured  $S_{h\min}$  (red bars) and estimated  $S_{h\max}$  (blue bars) magnitude ranges along the TRU1-1 and MAR1-1 borehole trajectories in Fig. 5. In our study, since the fault agnostic models are compared against the REF model, we first look at the results of the REF model in isolation before examining the results from all the four model realizations together.

In general, the predicted horizontal stress magnitudes from the REF model (Fig. 5; vertical red line changing with depth), align reasonably well with the measured stress ranges across different geomechanical units. However, some discrepancies are present, particularly in the Klettgau and Bänkerjoch formations, where the REF model underestimates  $S_{h\min}$  magnitudes, and in the Schinznach formation, where it overestimates  $S_{h\min}$  magnitude is overestimated. These deviations arise because the REF model uses P50 (median) stiffness values for stress simulations, whereas the MHF are representative of rock volume at a meter scale. Also, for the model calibration on with the measured horizontal stress magnitudes, the REF model uses P50 (median) horizontal stress magnitude values despite in spite of the MHF tests resulting in ranges (red and blue bars in Fig. 5). Therefore, the stress predictions may vary from the assumed P50 value at a particular point in the subsurface. The vertical

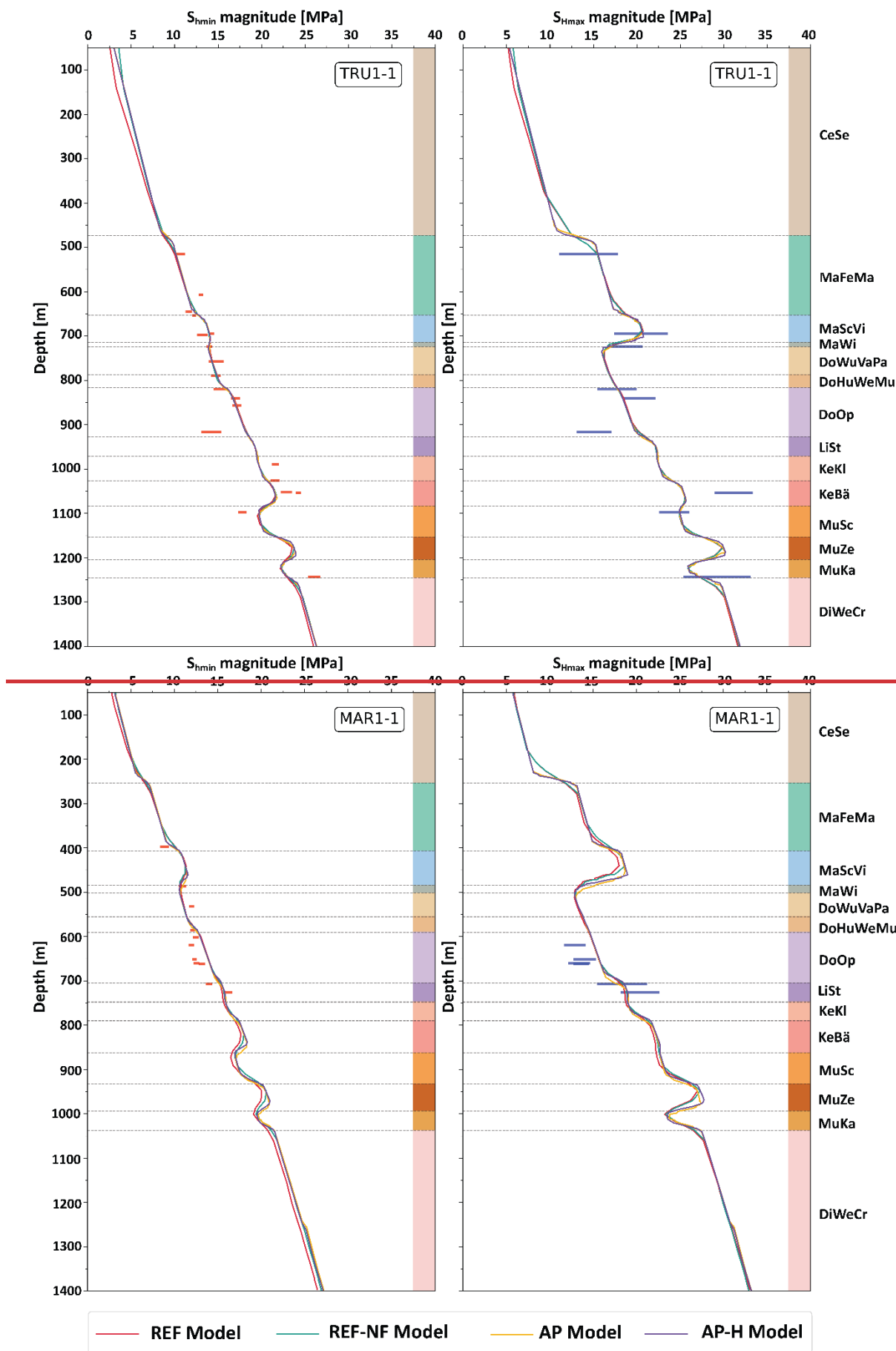
423 stress magnitude ( $S_v$ ) is calculated from the weight of the overlying rock mass, considering the densities of the  
424 individual lithologies. From Fig. 5, it can be seen that  $S_v$  increases linearly with depth.

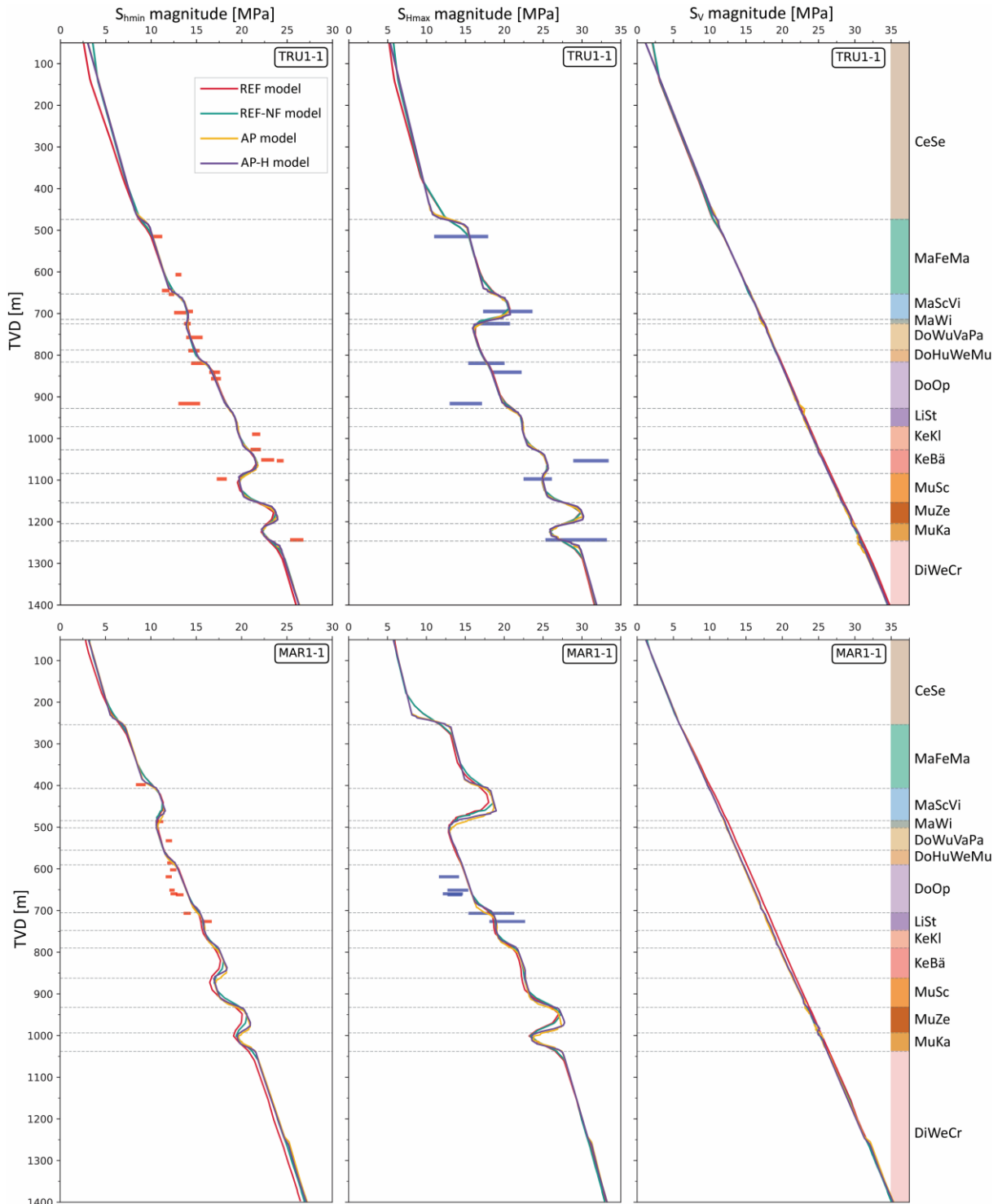
425 The predicted results from all the model realizations, regardless of fault implementation or exclusion, also align  
426 well with the measured horizontal stress magnitude ranges along both borehole trajectories across different  
427 geomechanical units, and are consistent with the REF model. Minor but negligible differences of <1 MPa in the  
428  $S_{Hmax}$  magnitudes can be found at ~475 m (t.v.d) along the TRU1-1 borehole and at ~250 m (t.v.d) along the  
429 MAR1-1 borehole in the AP and AP-H models (Fig. 5). This is likely due to a high stiffness contrast between the  
430 Cenozoic sediments ( $E = 15$  GPa) and Felsenkalke + Massenkalke ( $E = 31$  GPa) units, the transition boundary of  
431 which is differently discretized due to ApplePy usage. A similar difference can be found at the Zeglingen Fm. ( $E =$   
432 36 GPa), Kaiseraugst Fm. ( $E = 23$  GPa) and the Dinkelberg, Weitenau Fm. and Crystalline basement ( $E = 34$  GPa),  
433 which is also due to the widely varying stiffness contrasts.

434 Stiffer formations such as the Schwarzbach-Villigen Fm., Zeglingen Fm., and the basement have broader stress  
435 ranges in the measured data due to their statistically larger stiffness variability, while weaker formations like the  
436 Opalinus Clay exhibit narrower, more consistent stress distributions. Moreover, stiffer layers shield the weaker  
437 layers above and below, reducing stress variability in these formations. In short, Fig. 5 clearly indicates that the  
438 differences between the profiles from all the models are smaller than the measurement errors, represented by  
439 the length of the horizontal red and blue bars, and that the differences between the fault agnostic models and  
440 the REF model are insignificant. The variation of  $S_v$  magnitude with depth is consistent across all the model  
441 realizations, with differences <0.05 MPa observed between the models using ApplePy and the standard  
442 procedure.

443 The AP and AP-H models yield identical results. This indicates that increasing model resolution would not  
444 significantly improve stress predictions in our study and that the resolution of the AP model is already sufficient.  
445 This rules out resolution effects within the ApplePy models on the predicted stress magnitudes with respect to  
446 the REF model.

447





449

450 Figure 5: Measured and modelled  $S_{h\min}$  magnitude, and  $S_{h\max}$  magnitudes, and  $S_v$  magnitude ranges of all the model  
 451 realizations with depth (TVD.t.v.d) along the borehole trajectories of TRU1-1 (top row) and MAR1-1 (bottom row) borehole.  
 452 The horizontal red bars represent the lower upper ranges of the  $S_{h\min}$  magnitude and horizontal blue bars represent the  
 453 lower upper ranges the  $S_{h\max}$  magnitudes. The red and blue horizontal bars show the measured in-situ stress magnitude data  
 454 of the  $S_{h\min}$  and  $S_{h\max}$ , with lengths indicating their individual uncertainty (Nagra, 2024d, c). The geomechanical units are  
 455 represented by their respective colors and abbreviations, consistent with Fig. 3 and Table 1.

456 The predicted results from all the model realizations, regardless of fault implementation or exclusion, also align  
 457 well with the measured horizontal stress magnitudes ranges along both the borehole trajectories across different  
 458 geomechanical units and also with respect to the REF model. Little but negligible differences of < 1 MPa in the  
 459  $S_{h\max}$  stress magnitudes can be found at  $\sim 475$  m (t.v.d) along the TRU1-1 borehole and at  $\sim 250$  m (t.v.d) along  
 460 the MAR1-1 borehole in the AP and AP-H models (Fig. 5). This is likely due to a high stiffness contrast between

461 the Cenozoic Sediments ( $E = 15$  GPa) and Felsenkalke + Massenkalk ( $E = 31$  GPa) units, the transition boundary  
462 of which is differently discretized due to ApplePy usage. Another such difference can be found at the Zeglingen  
463 Fm. ( $E = 36$  GPa), Kaiseraugst Fm. ( $E = 23$  GPa) and the Dinkelberg, Weitenau Fm. and Crystalline basement ( $E =$   
464  $34$  GPa), which is also due to the widely varying stiffness contrasts. While the P50 values of the horizontal stress  
465 magnitudes fit well across all the predicted horizontal stress magnitudes, local deviations occur due to presence  
466 of geomechanical anomalies. For instance, stress magnitude data at 916 m (t.v.d) in TRU1-1 reflect lower stiffness  
467 (Young's modulus  $\sim 3$  GPa) at the measurement site, compared to the typical 11 GPa of the Opalinus Clay (Fig. 5).  
468 This particular measurement was taken within a weak lens in the Opalinus Clay and is not accounted for by our  
469 models due to the assumptions made while setting up the models. In general, stiffer formations such as the  
470 Schwarzbach-Villigen formation, Zeglingen formation and the basement have broader stress ranges in the  
471 measured data due to their statistically larger stiffness variability, while weaker formations like the Opalinus Clay  
472 exhibit narrower, more consistent stress distributions. Moreover, stiffer layers shield the weaker layers above  
473 and below, reducing stress variability in these formations. In short, Fig. 5 clearly indicates that the differences of  
474 the profiles from all the models are smaller than the measurement errors, represented by the length of the  
475 horizontal red and blue bars, and that the differences between the fault agnostic models and the REF model are  
476 insignificant.

477  
478  
479

480 The AP and AP H models yield identical results. This indicates that increasing model resolution would not  
481 significantly improve stress predictions in our study and that the resolution of the AP model is already sufficient.  
482 This rules out resolution effects within the ApplePy models on the predicted stress magnitudes with respect to  
483 the REF model.

## 484 4.2 Model 2D results along a vertical-a cross-section and a horizontal layer

### 485 4.2.1 Spatial variation of horizontal differential stresses ( $S_{Hmax}-S_{hmin}$ )

486 Along the W-E cross-section through borehole TRU1-1, the horizontal differential stress ( $S_{Hmax}-S_{hmin}$ ) of the four  
487 models displayed in Fig. 6a-d shows only small differences, except near the contact surfaces where noticeable  
488 localized stress concentrations in the REF model occur. Similar result shows up when comparing the values of  
489  $S_{Hmax}-S_{hmin}$  along the mean Opalinus clay layer from the REF model (Fig. 6e) with those of REF-NF model (Fig. 6f).  
490 To quantify the difference of the three fault-agnostic models w.r.t the REF model, Fig. 7a-c displays the difference  
491 in the horizontal differential stress  $\Delta(S_{Hmax}-S_{hmin})$  between the models. The values of  $\Delta(S_{Hmax}-S_{hmin})$  exceed  $\pm 2$  MPa  
492 only within 100 m of the fault. Beyond approximately 200 m from the faults,  $\Delta(S_{Hmax}-S_{hmin})$  across all models  
493 becomes more similar to each other, and differences relative to the REF model typically remain below  $\pm 0.4$  MPa.  
494 As the distance from the faults increases, the value of  $\Delta(S_{Hmax}-S_{hmin})$  differences rapidly decreases.

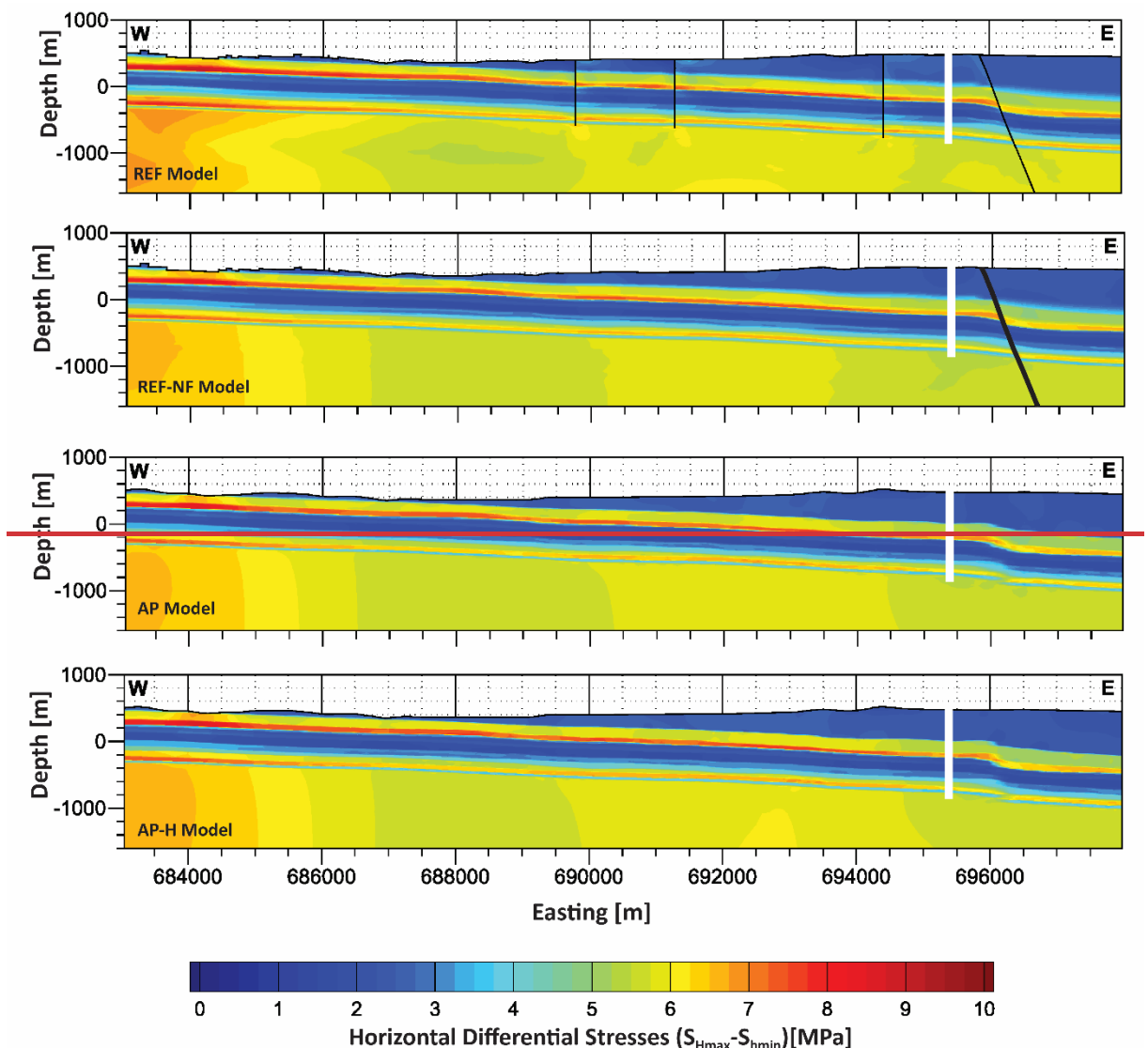
495 In addition to the spatial proximity to contact surfaces, the variation of  $S_{Hmax}-S_{hmin}$  depends on the stiffness of the  
496 geomechanical units. In specific Mesozoic units characterized by lower stiffness, such as from the Wildegg Fm.  
497 of the Malm Group to the Klettgau Fm. of the Keuper group, and the Kaiseraugst Fm. of the Muschelkalk group  
498 (Table 1), the  $S_{Hmax}-S_{hmin}$  typically is  $< 3.5$  MPa. In contrast, units with high stiffness can exhibit  $S_{Hmax}-S_{hmin}$   
499 exceeding 7 MPa, such as in the «Felsenkalke» + «Massenkalk» and the Schwarzbach-Villigen Fm. of the Malm  
500 group, Schinznach and Zeglingen Fm. of the Muschelkalk group and the Dinkelberg Fm., Weitenau Fm. and  
501 Crystalline basement (Fig. 6a-d, Table 1). This trend is expected, as lower stiffness materials accommodate  
502 deformation more readily, resulting in lower differential stresses, whereas stiffer units resist deformation,  
503 leading to higher differential stresses. The Opalinus Clay layer has a Young's modulus of 11 GPa, which is relatively  
504 low compared to the other geomechanical units present in the siting region. The adjacent stiffer geomechanical  
505 units act as stress-bearing members, effectively shielding the soft layer and further reducing the stress  
506 magnitudes concentrated within it. The  $S_{Hmax}-S_{hmin}$  in the mean Opalinus Clay layer, as predicted by the models,  
507 is  $< 2$  MPa irrespective of fault inclusion or exclusion from the model (Fig. 6e-f).

508 A particularly notable observation is that the differential stress near the Neuhausen fault remains relatively  
509 comparable across all models when compared to the magnitude of differences in  $S_{h\max}$ - $S_{h\min}$  at other contact  
510 surfaces. Despite the Neuhausen fault being either fully removed or mechanically disabled via a high friction  
511 coefficient, the differential stress pattern across the 50-meter offset between the footwall and the hanging wall  
512 is well replicated in the AP and the AP-H models in Fig. 6a-d. This is attributed to the abrupt contrast in mechanical  
513 properties across the Neuhausen Fault (Fig. 3; Table 1), which effectively mimics the local stress response, even  
514 in the absence of explicit fault representation.

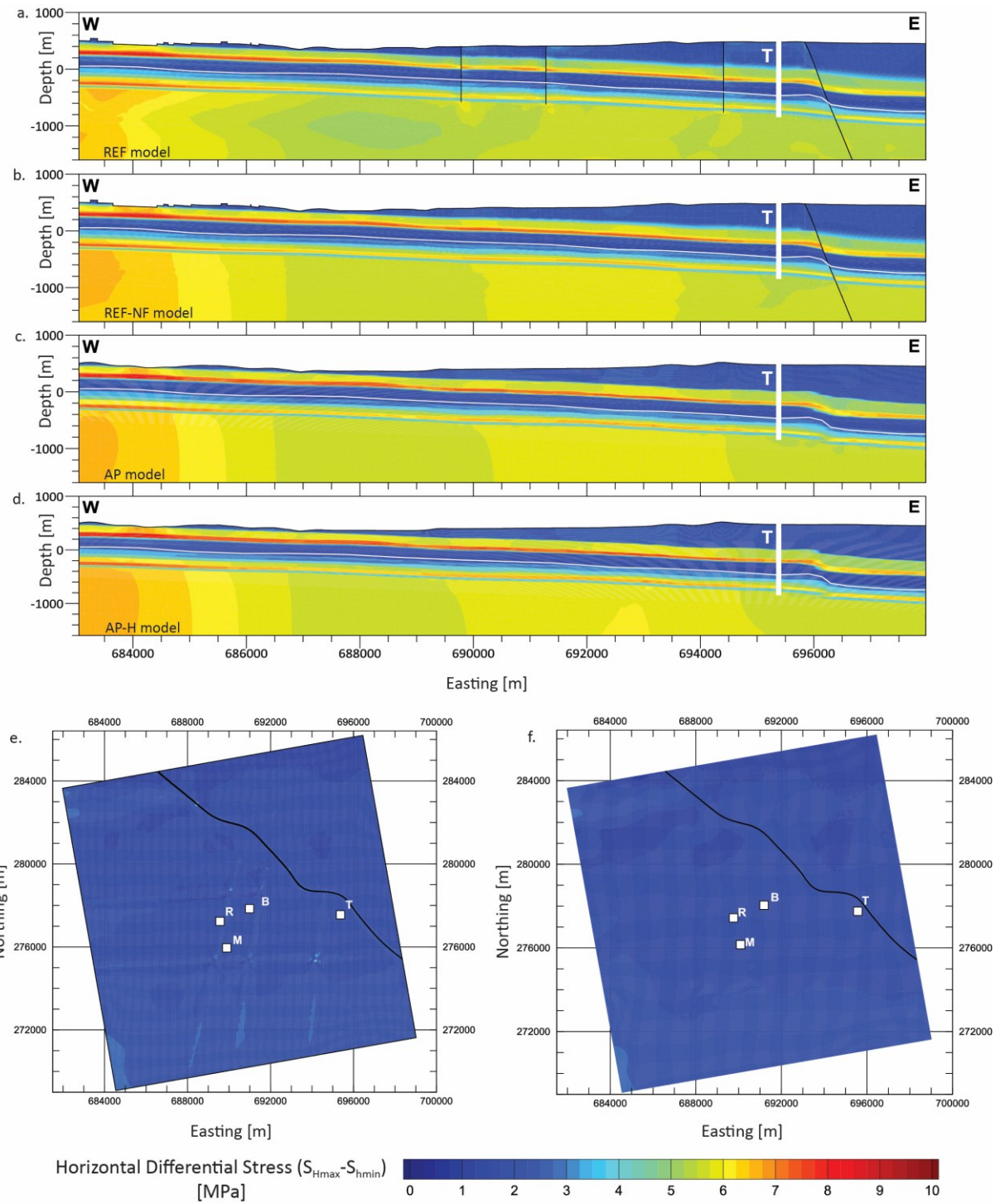
515 Fig. 6 illustrates the spatial variation of horizontal differential stresses ( $S_{h\max}$ - $S_{h\min}$ ) for all model realizations along  
516 a W-E cross section and Fig. 7 illustrates the corresponding quantitative differences relative to the REF model,  
517 along the same cross section. In the cross sections in Fig. 6,  $S_{h\max}$ - $S_{h\min}$  visually appears consistent between  
518 different model realizations, except near the contact surfaces where noticeable localized stress concentrations  
519 in the REF model occur (Fig. 7). The contact surfaces are not included in the fault agnostic models (REF, NF, AP,  
520 and AP-H), which explains the larger differences in differential stresses ( $\Delta(S_{h\max}$ - $S_{h\min}$ ) observed. The  $\Delta(S_{h\max}$ -  
521  $S_{h\min}$ ) exceeds  $\pm 2$  MPa within 100 m of the fault, technically the contact surfaces. Beyond approximately 200 m  
522 from the contact surfaces,  $\Delta(S_{h\max}$ - $S_{h\min}$ ) across all models become more similar to each other, and differences  
523 relative to the REF model typically remain below  $\pm 0.4$  MPa, less than the average widths of the measured stress  
524 magnitude ranges shown in Fig. 5. As distance from the contact surfaces increases, the magnitude of the  $\Delta(S_{h\max}$ -  
525  $S_{h\min}$ ) differences rapidly decreases. It is important to note that variations in the stress field occurring over lateral  
526 distances smaller than 60 m cannot be numerically resolved in our models, as the minimum lateral resolution is  
527 about 60–80 m in the AP-H model and approximately 80–150 m in the other model realizations (Table 2).

528 In addition to the spatial proximity to contact surfaces, the variation of  $S_{h\max}$ - $S_{h\min}$  depends on the stiffness of the  
529 geomechanical units. In specific Mesozoic units characterized by lower stiffness, such as from the Wildegg Fm.  
530 of the Malm Group to the Klettgau Fm. of the Keuper group, and the Kaiseraugst Fm. of the Muschelkalk group  
531 in the order shown in Table 1, the  $S_{h\max}$ - $S_{h\min}$  typically is  $< 3.5$  MPa. In contrast, units with high stiffness can exhibit  
532  $S_{h\max}$ - $S_{h\min}$  exceeding 7 MPa, such as in the «Felsenkalke» + «Massenkalk» and the Schwarzbach-Villigen Fm. of  
533 the Malm group, Schinznach and Zeglingen Fm. of the Muschelkalk group and the Dinkelberg Fm., Weitenau Fm.  
534 and Crystalline basement (Fig. 6, Table 1). This trend is expected, as lower stiffness materials accommodate  
535 deformation more readily, resulting in lower differential stresses, whereas stiffer units resist deformation,  
536 leading to higher differential stresses.

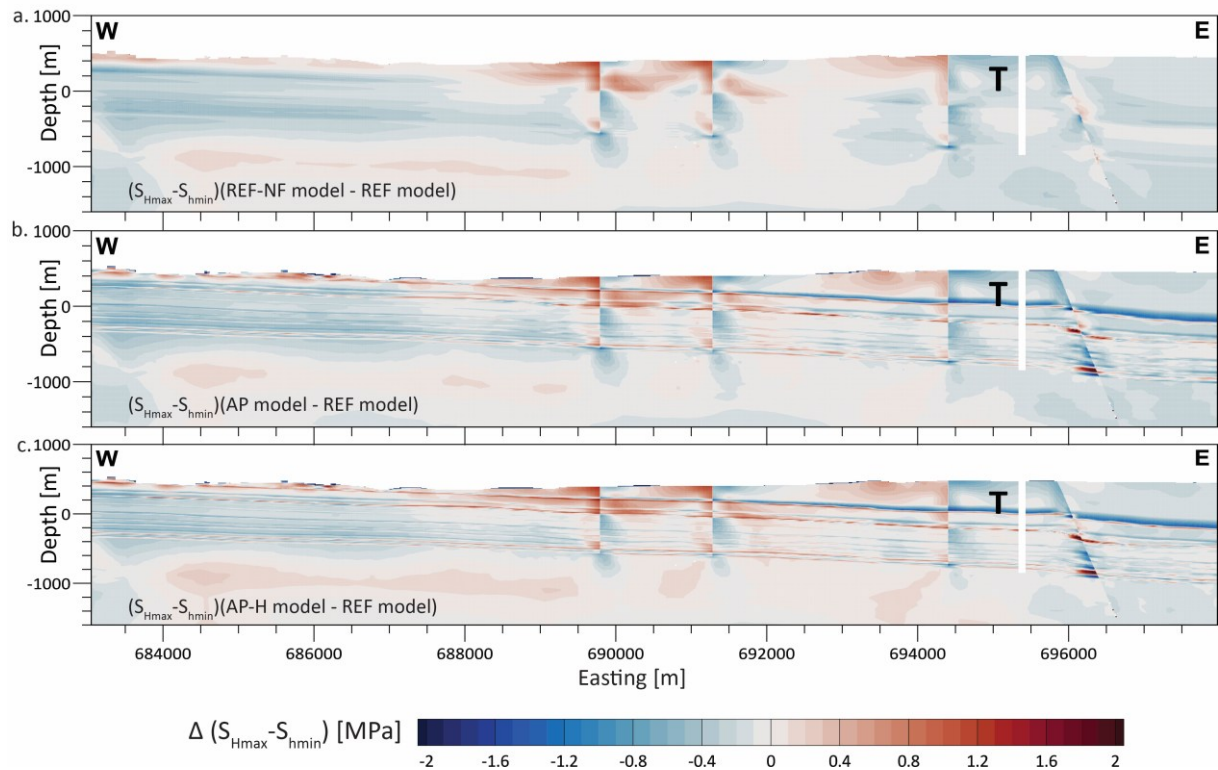
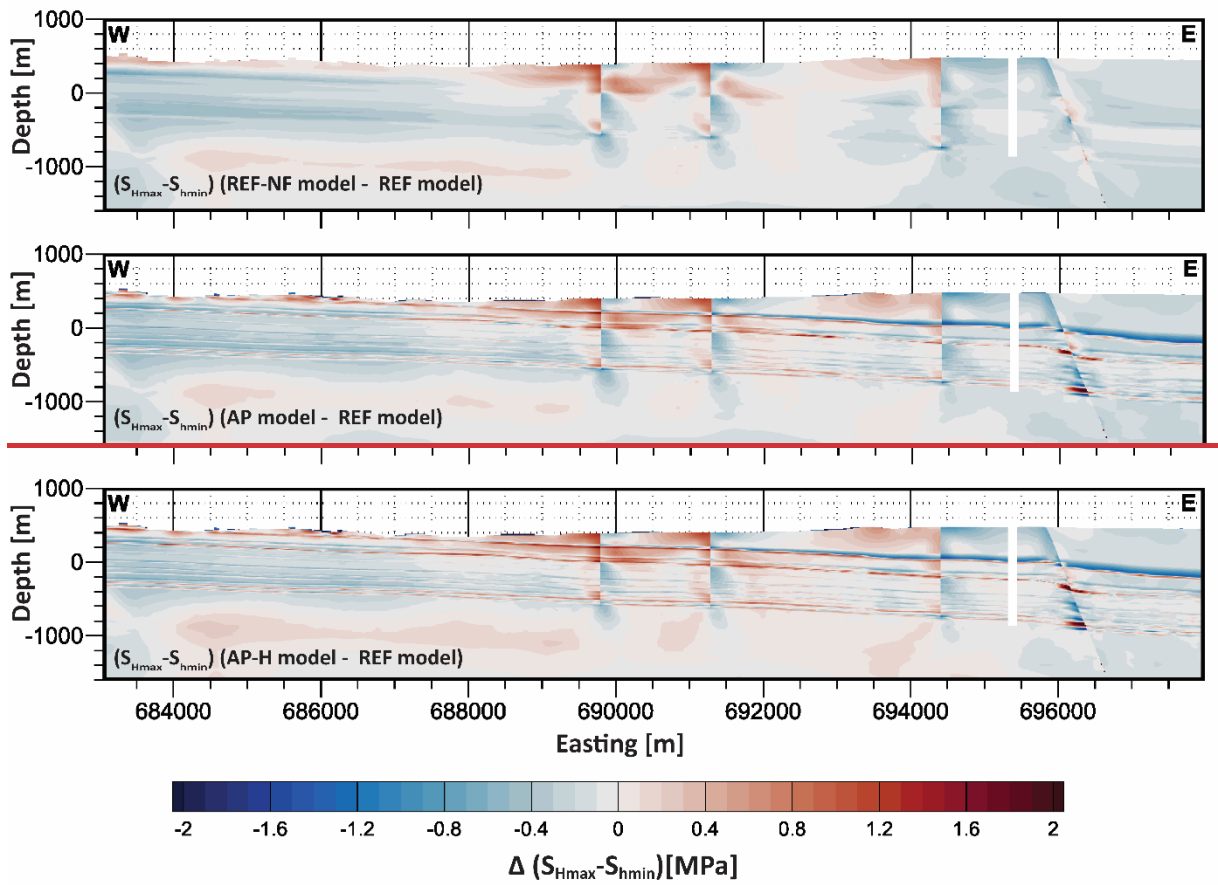
537 A particularly notable observation is that the differential stress near the Neuhausen fault remains relatively  
538 comparable across all models when compared to the magnitude of differences in  $S_{h\max}$ - $S_{h\min}$  at other contact  
539 surfaces. Despite the Neuhausen fault being either fully removed or mechanically disabled via a high friction  
540 coefficient, the differential stress pattern across the 50-meter offset between the footwall and the hanging wall  
541 is well replicated in the AP and the AP-H models in Fig. 6. This is attributed to the abrupt contrast in mechanical  
542 properties across the Neuhausen Fault (Fig. 3; Table 1), which effectively mimics the local stress response, even  
543 in the absence of explicit fault representation.



544



545  
546 **Figure 6: a-d)** Comparison of the **h** Modelled horizontal differential stress ( $S_{hmax} - S_{hmin}$ ). a-d) W-E cross section (brown line in  
547 Fig. 2) through the TRU1-1 borehole (white vertical bar) with depths referenced to below sea level (b.s.l.). The location of  
548 faults is indicated by black lines. e-f) Mean Opalinus Clay layer of the REF and REF-NF model, indicated by the white lines on  
549 the W-E cross sections. Capital letters indicate the location of the four boreholes TRU1-1 (T), BEN (B), MAR1-1 (M), and RHE1-  
550 1 (R). horizontal differential stresses ( $S_{hmax} - S_{hmin}$ ) along a W-E profile passing through TRU1-1 borehole (white blank space) and  
551 a fixed Northing = 277548 m. The depths are referenced to the mean sea level (m.s.l.). Higher  $S_{hmax} - S_{hmin}$  is observed in stiffer  
552 units whereas lower  $S_{hmax} - S_{hmin}$  are observed in units with lower stiffness. The location of faults is indicated by black lines,  
553 similar to Fig. 3. In the REF-NF model, the thickness of the Neuhausen fault is increased to signify that the fault has been  
554 mechanically deactivated by increasing the friction coefficient to 50, leading to no allowed slip/displacement along it.



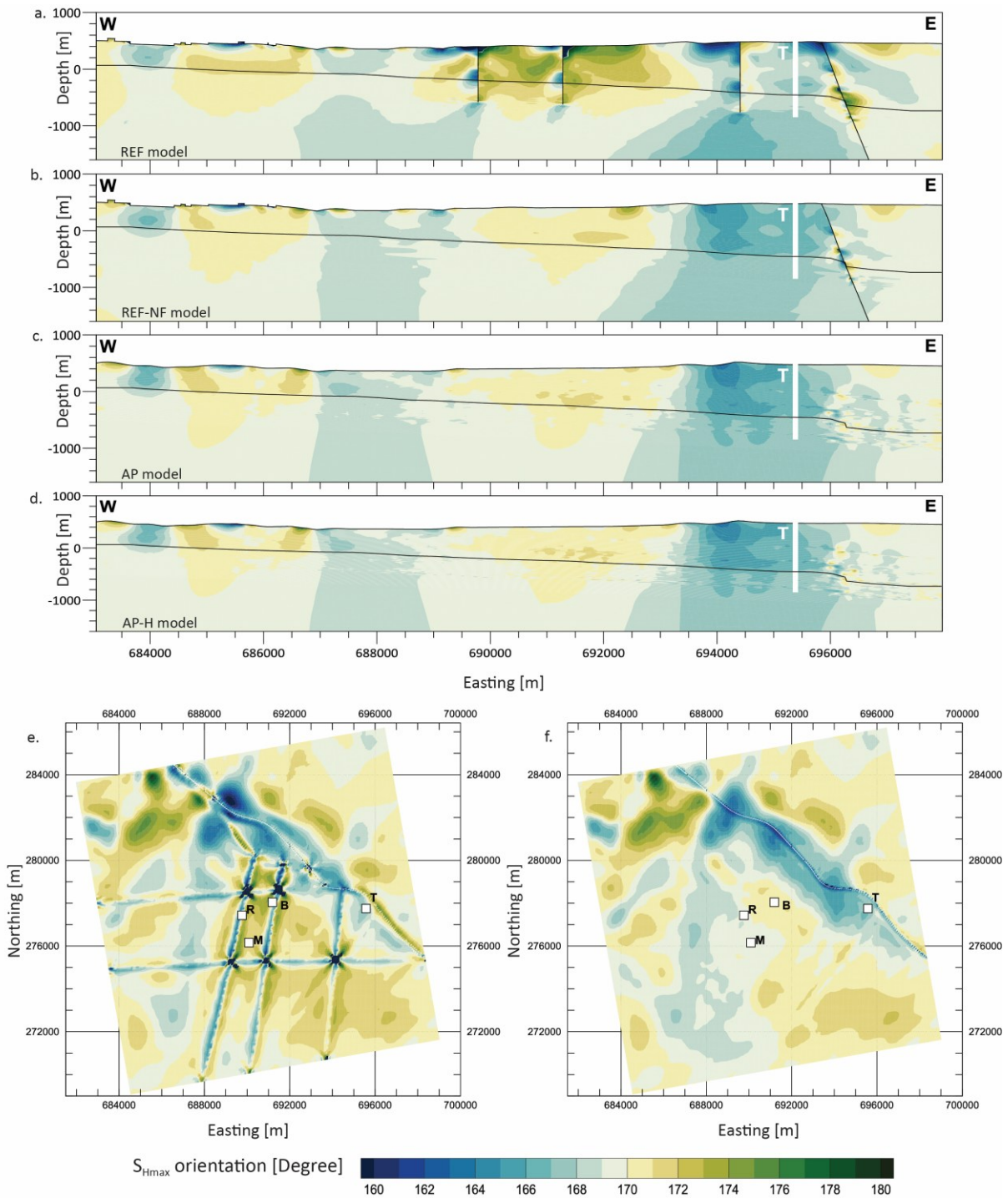
557 Figure 7: a-c: Comparison of the  $\Delta (S_{Hmax} - S_{hmin})$  between the models without faults and the REF model with  
 558 active faults along the same cross-section as in Fig. 6. The cross-sectionslices show the difference with respect to the REF  
 559 model and are indicated at the bottom left of each slice. Key differences are primarily concentrated near contact surfaces  
 560 within approximately 100 m. Although faults have not been directly indicated on the cross-sections, the location of the faults  
 561 can be visually seen as sudden lateral changesdiscontinuities in an otherwise continuous change in  $\Delta (S_{Hmax} - S_{hmin})$ . Visually,  
 562 the individual geomechanical layers becomes more apparent in the two ApplePy models: AP and AP-H. This is due to the step-

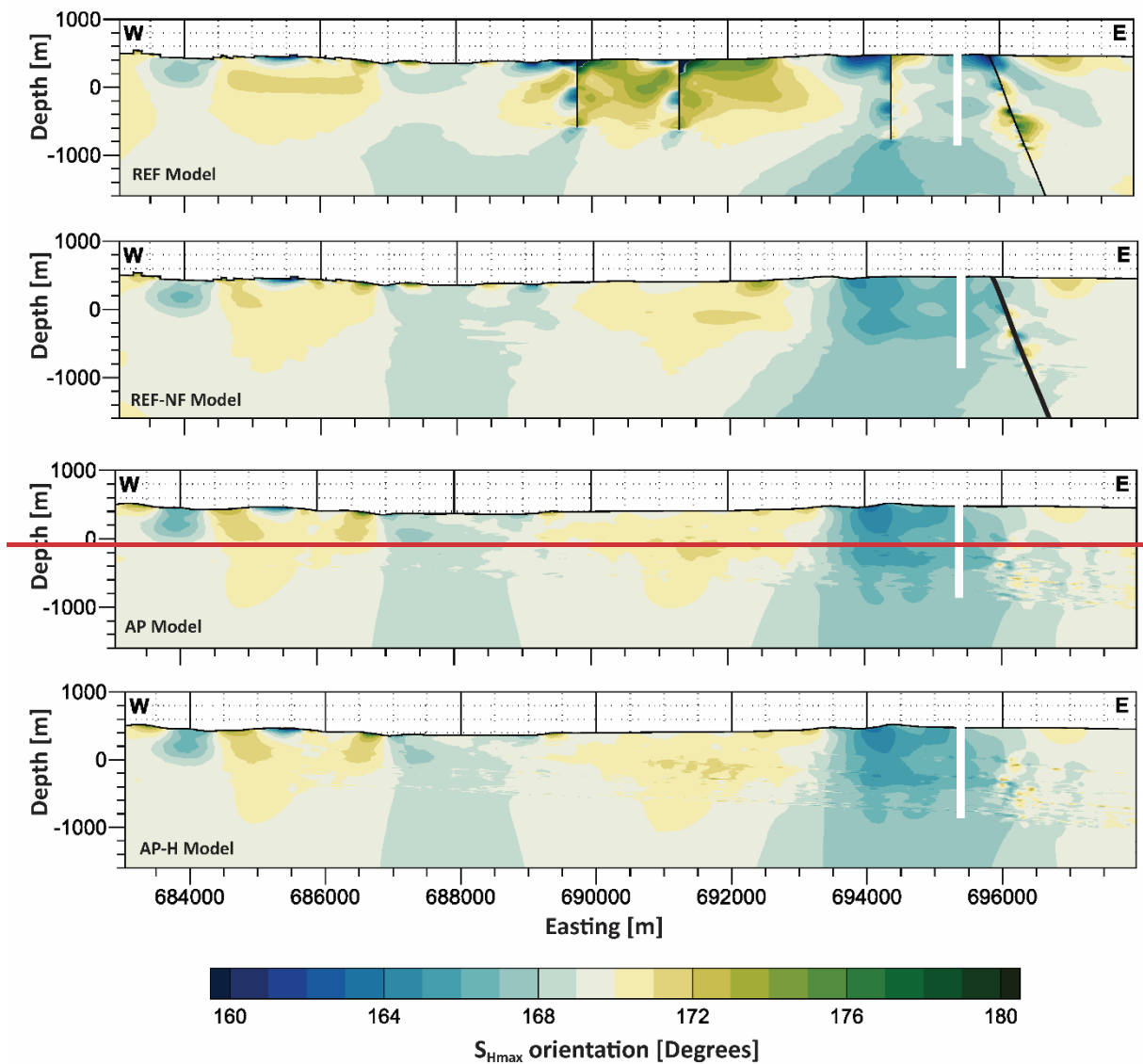
563 like transition between a higher stiffness geomechanical unit and a lower stiffness geomechanical unit, leading to a more  
564 prominent visibility of stiffness contrasts at the geomechanical unit transitions.

#### 565 4.2.2 ~~Spatial variation of~~ $S_{H\max}$ orientation

566 ~~Along the same W-E cross-section as in Fig. 6a-d, in addition to  $S_{H\max}$ - $S_{h\min}$ , we also examined the the  $-S_{H\max}$~~   
567 ~~orientation of the four models is displayed in (Fig. 8a-d, and the variability of the  $S_{H\max}$  orientation w.r.t the REF~~  
568 ~~model is displayed in ) and its variability along the same W-E cross-section (Fig. 9a-c). Fig. 8e-f shows the variability~~  
569 ~~of  $S_{H\max}$  orientation along the mean Opalinus clay layer from the REF model and the REF-NF model respectively.~~

570 The largest  $S_{H\max}$  orientation variability is reoriented more within a distance of 100–200 m around the contact  
571 surfaces, similar to the observations of  $\Delta(S_{H\max}-S_{h\min})$ . At this distance, differences greater than 6° w.r.t. the REF  
572 model are observed (Fig. 10). These differences tend to reduce to less than  $\pm 2^\circ$  at lateral distances greater than  
573 500 m from the contact surfaces. Within the near-field zone, which is <300 m from the contact surfaces, stress  
574 concentrations are probably artifacts arising from ~~the numerical resolution limits of the finite elements, which~~  
575 ~~means that the values within 60–100 m from the contact surfaces should be interpreted with caution. This shift~~  
576 ~~in  $S_{H\max}$  orientation can also be observed in Fig. 8e-f along and near the contact surfaces. Even under a~~  
577 hypothetical assumption that the observed variations are entirely fault-induced,  ~~$S_{H\max}$ -orientation changes are~~  
578 ~~within 10° relative to the regional trend. Given that the current stress indicator techniques cannot resolve  $S_{H\max}$~~   
579 ~~variations within 10°. Therefore, ns with a corresponding precision, these differences can be considered in are~~  
580 ~~not significant and non-resolvable. Finally, increasing model resolution does not change our results, as seen when~~  
581 comparing the ~~AP and AP-Htwo ApplePy~~ model results in Fig. 8 and Fig. 9.

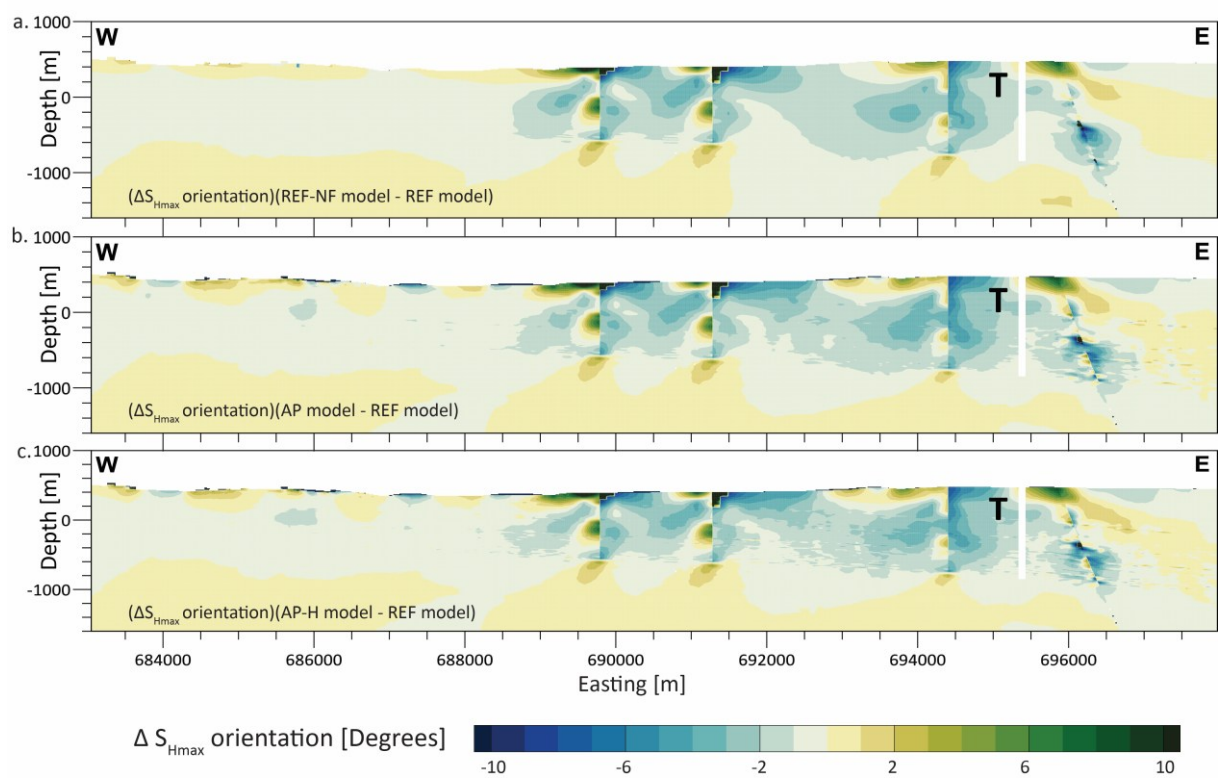
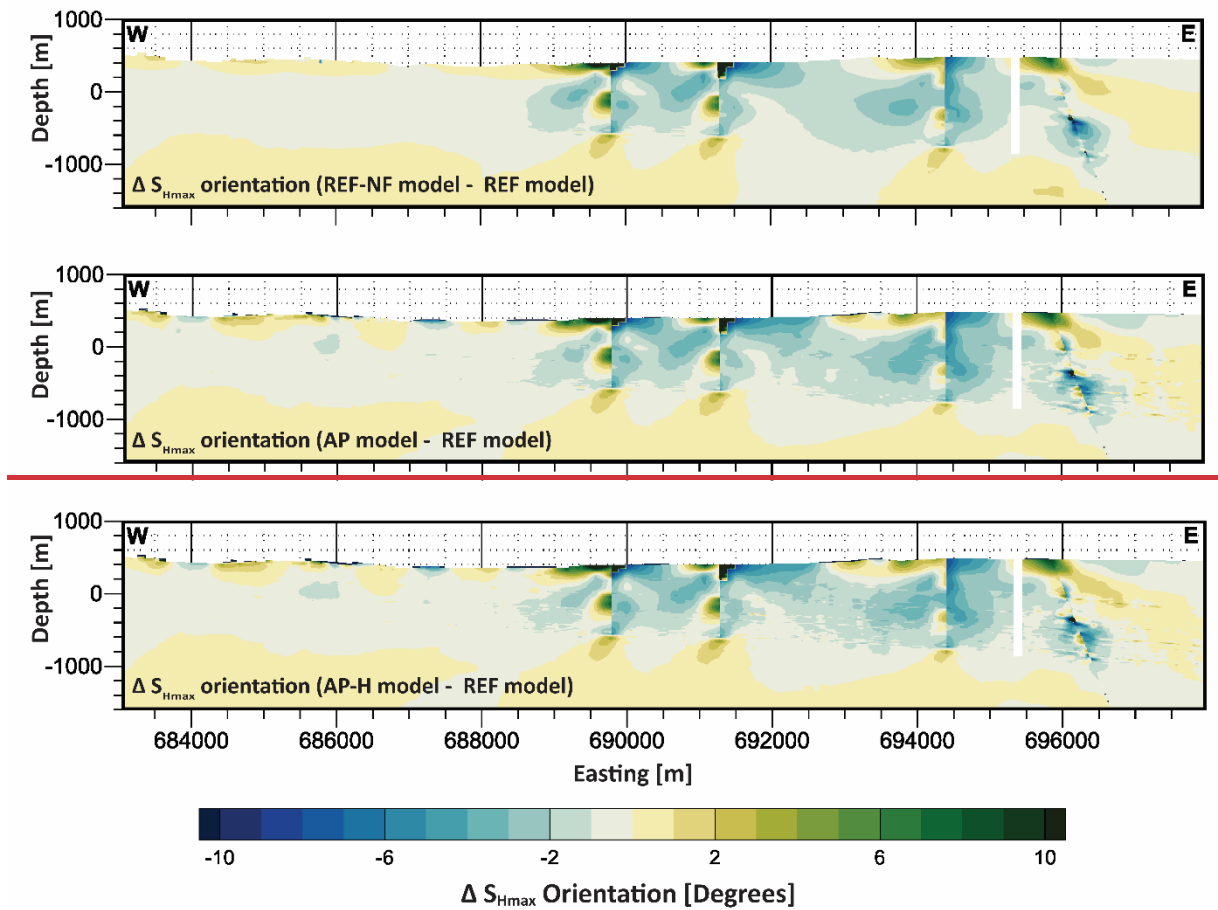




583  
584  
585  
586  
587  
588  
589  
590  
591

Figure 8: Absolute S<sub>Hmax</sub> orientation. a-d) W-E cross-section through borehole TRU1-1 (T) indicated with the white vertical bar. e-f) Mean Opalinus Clay layer of the REF and REF-NF model, indicated by the black lines on the W-E cross sections. Capital letters indicate the location of the four boreholes TRU1-1 (T), BEN (B), MAR1-1 (M), and RHE1-1 (R).

Figure 8: Comparison of the absolute S<sub>Hmax</sub> orientation along the same profile as in Fig. 6 and 7. The white black space indicates the TRU1-1 borehole. The location of faults is indicated by black lines, similar to Fig. 3. In the REF-NF model, the thickness of the Neuhausen fault is increased to signify that the fault has been mechanically deactivated by increasing the friction coefficient to 50, leading to no allowed slip/displacement along it.



599 differences are primarily concentrated near contact surfaces within approximately 100–200 m. Note that the range of the  
600 color scale is smaller than the uncertainties of the stress orientation data records from the best stress indicator techniques  
601 i.e., Borehole Breakouts (BO) and Drilling induced tensile fractures (DITF).

602 4.3 Quantification of the lateral extent of fault-induced stress changes.

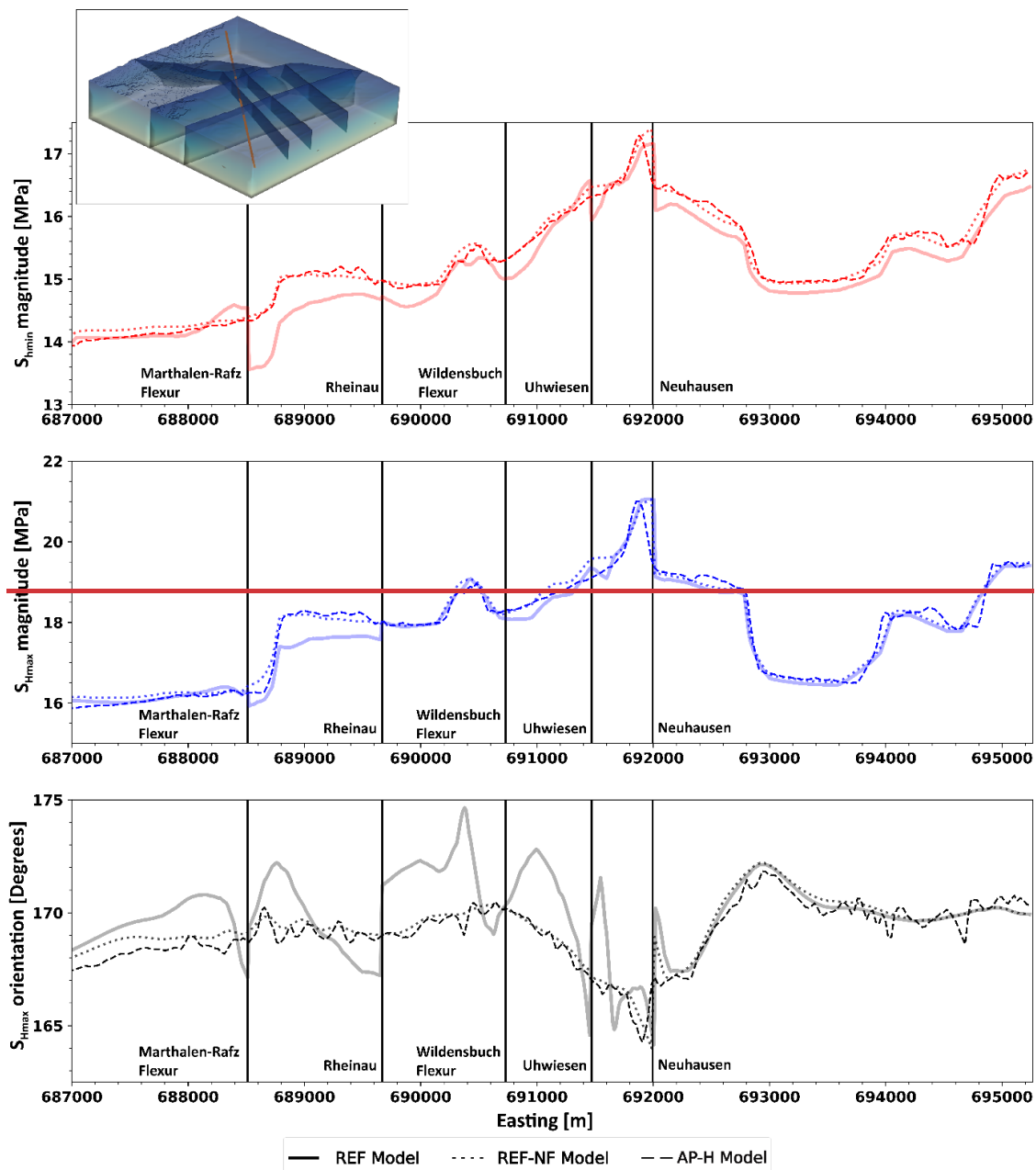
603 To better quantify the impact of faults on stress, we interpolated the results of the four models on a SW-NE  
604 oriented horizontal line at 300 m (b.s.l) crossing five of the seven faults (Fig. 10a-c). To further investigate the  
605 spatial extent of fault impact on the stress state, we analyzed the lateral variation of stress tensor components  
606 by comparing results from different model realizations. For this purpose, stress values were extracted along a  
607 SW-NE oriented horizontal line located at a depth of 300 m (b.s.l). The horizontal line has been chosen such that  
608 it passes through as many fault structures as possible. The results of this comparison are presented in Fig. 10. To  
609 improve readability, the results from the AP model were not plotted, as it is clear from Fig.-s. 5, 7, and 9 that the  
610 that AP and AP-H model results are almost identical.

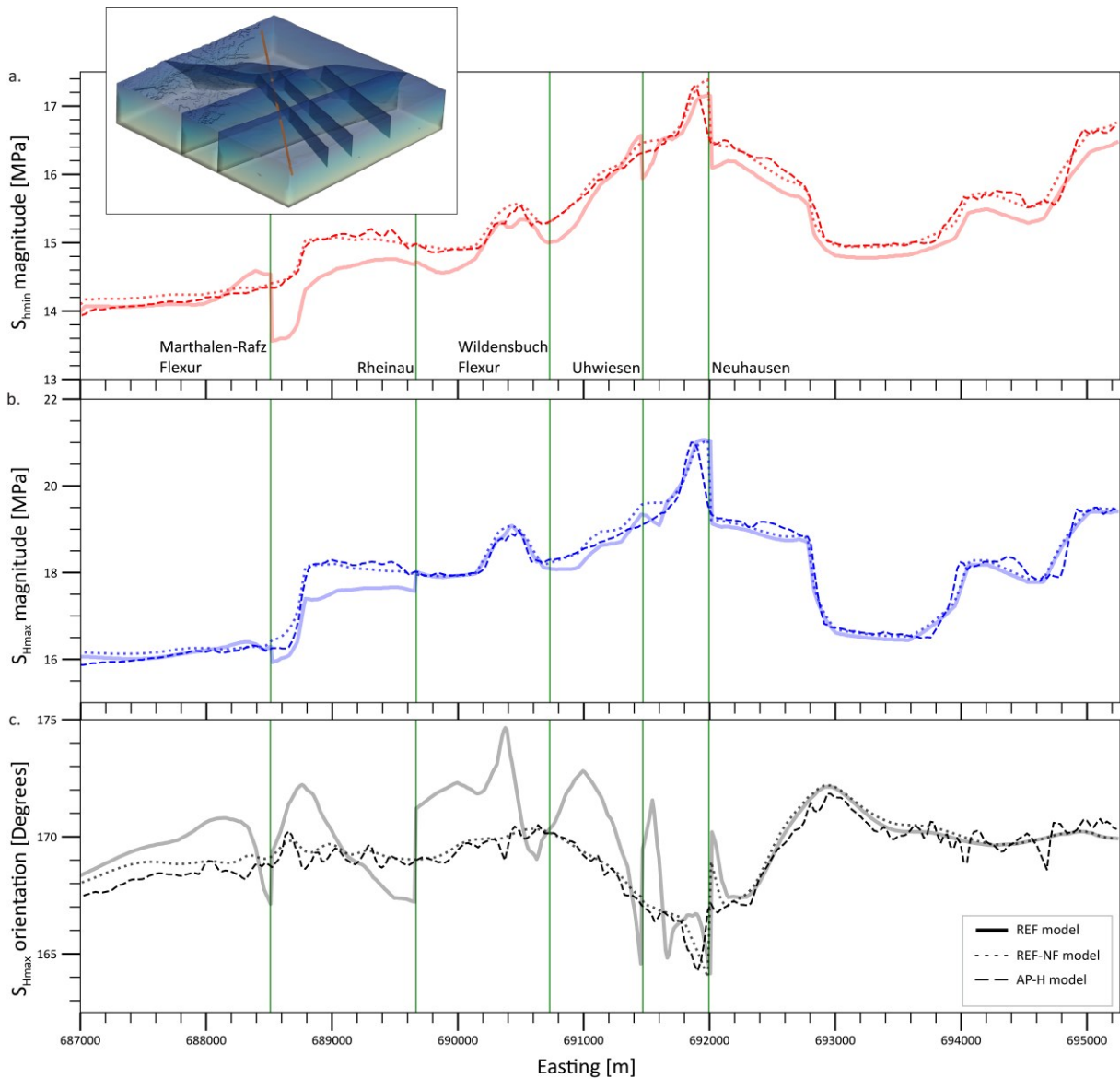
611 The  $S_{H\max}$  and  $S_{h\min}$  magnitudes of different model realizations largely overlap each other along the horizontal  
612 line. (Fig. 10). A difference of  $\sim 0.5$  MPa is observed in  $S_{H\max}$  magnitude (Fig. 10b), and  $\sim 1$  MPa is observed in the  
613  $S_{h\min}$  magnitudes (Fig. 10a) between the REF-mModel and the fault-agnostic models, within  $\sim 500$  m toof the  
614 faults. However, these differences are less than the widths of the stress magnitude measurement rangesdata,  
615 which in turn, represent the uncertainty of the measurements (Fig. 5). In general, the horizontal stress  
616 magnitudes from the REF model have an abrupt change in the vicinity of the faults, deviating from the continuous  
617 trend followed by other model realizations. The differences in the  $S_{H\max}$  magnitudes reduce to  $< 0.2$  MPa beyond  
618 a distance of about 500 m away from the fault. The differences in the  $S_{h\min}$  magnitudes follow the same pattern  
619 as the  $S_{H\max}$  magnitude, and also reduce beyond a distance of about 500 m away from the fault.

620 Similarly, the  $S_{H\max}$  orientation of the REF model shows negligible deviations of  $< 2^\circ$  in the undisturbed rock  
621 volume, away from the faults, and a deviation of  $2^\circ$ – $6^\circ$  up to 1 km from the modeled faults (Fig. 10c). According  
622 to the quality ranking scheme of the  $S_{H\max}$  orientation from the World Stress Map, the A-quality dataset, data of  
623 the highest quality, has an uncertainty a standard deviation of  $\pm 15^\circ$  (Heidbach et al., 2025a). Even  $S_{H\max}$   
624 orientations derived from the DITF and BO in the MAR1-1 and TRU1-1 boreholes exhibit standard deviations of  
625 approximately  $\pm 11^\circ$ . Considering this, the orientation deviations seen in Fig. 10c are not resolvablenegligible and  
626 well below the uncertainties of the in situ indicators.

627 Near the Neuhausen fault, there is a localized abrupt change in the stress tensor componentshorizontal stress  
628 magnitudes within  $\sim 100$  m on either side of the modelled fault for all the model realizations. An important  
629 observation is that this abrupt change occurs not only in the REF model but also in the models without any faults.  
630 These stress changes are primarily controlled by the lateral stiffness contrasts due to the offset and not by the  
631 mere presence of the faults.

632 Overall, the differences are  $< 0.2$  MPa in stress magnitudes and  $< 2^\circ$  in  $S_{H\max}$  orientations beyond 1 km from the  
633 fault, which is far less than the uncertainties of the horizontal stress magnitude measurementsdata from the  
634 MHF and the SR tests, as well as the stress indicators for the  $S_{H\max}$  orientation from the boreholes. Even in a  
635 conservative approach, it is clear that the effect of faults on the stress field is within about 1 km from the fault  
636 core. This conclusion aligns with the findings by Reiter et al. (2024), who, through generic model studies, found  
637 that significant stress changes due to faults only occur within a distance of a few hundred meters, partly up to 1  
638 km next to the fault.





640  
641 Figure 10: Magnitudes of  $S_{H\min}$  and  $S_{H\max}$ , and the  $S_{H\max}$  orientation along a SW-NE horizontal profile at 300 m (b.s.l.), shown  
642 in the 3D figure as a red line. Green vertical lines with the respective fault names denote the location where the profile crosses  
643 the modelled faults.

644 Effects of faults on Stress tensor components along a SW-NE horizontal line at 300 m (bsl). The location where the horizontal  
645 profile meets the modelled faults are denoted by black vertical lines with the respective fault names. The red color lines  
646 represent the  $S_{H\min}$ -magnitude, blue represent the  $S_{H\max}$ -magnitude and black represent the  $S_{H\max}$ -orientation. The line styles  
647 represent different model realizations. Note that the value of the y axis is different for each sub plot. Notice that there is an  
648 abrupt change in the profile in all model realizations, at the Neuhausen fault, indicating that stress changes are caused by  
649 lateral stiffness contrasts and not by the 'mere' fault presence. The location of the horizontal line, indicated in red, is shown  
650 in the 3D insert at the top left.

651 5. Discussion

652 5.1 Comparison with observed  $S_{H\max}$  orientation data

653 The orientation of the maximum horizontal stress ( $S_{H\max}$ ) orientation is the most widely available  
654 characteristic component of the reduced stress tensor. It is also the easiest component to analyze because it can  
655 be averaged and visualized with respect to the fault on stress maps (Fig. 1). This topic was a subject of several  
656 earlier studies (Yale et al., 1993; Yale et al., 1994; Yale and Ryan, 1994; Yale, 2003; Rajabi et al., 2017c; Heidbach  
657 et al., 2018). The  $S_{H\max}$  orientation can be determined from different stress indicators, such as from direct  
658 borehole-based measurements indicators, earthquake focal mechanisms, geological indicators, or passive

659 seismic methods (Amadei and Stephansson, 1997; Zang and Stephansson, 2010; Heidbach et al., 2025a). Among  
660 these, direct borehole-based indicatorsdata such as borehole breakouts (BOs), drilling-induced tensile fractures  
661 (DITFs), and hydraulic fracturing (HFs)- are commonly consideredregardedastobe the most reliable techniques  
662 (Bell, 1996a; Zang and Stephansson, 2010).

663 In the ZNO study region, 11  $S_{H\max}$  orientation data records are available from HFs, DITFs, and BOs. The mean  $S_{H\max}$   
664 orientation from these data is  $170^\circ$  with a standard deviation of  $\pm 11^\circ$ (Nagra, 2024d, c; Heidbach et al., 2025b).  
665 The individual standard deviation of each data record is between  $\pm 9^\circ$  and  $\pm 19^\circ$ , indicating that rotations smaller  
666 than $\pm 11^\circ$  cannot be resolved. As the differences between the REF model and the three fault-agnostic  
667 modelsrealizationswithoutfaults as displayed in Fig. 9, isare smaller than  $\pm 10^\circ$ , the potential impact cannot be  
668 resolved with anythe stress indicator. Furthermore, most of the rotations observed are located closeintothe  
669 nearfieldof the fault. At a distance of 1000 m from atthe fault, the rotation is  $<\pm 2^\circ$  and thus clearly below the  
670 uncertaintiesofanymeasurementresolutionlimit.

671 The stress regime of the rock volume, by itself, would not have an influence on the  $S_{H\max}$  orientation. A rotation  
672 of  $S_{H\max}$  orientation would primarily be driven by the horizontal differential stresses, i.e., the greater the  
673 horizontal differential stresses, the lesser the possibility of any rotation in the  $S_{H\max}$  orientation. (Bell, 1996a;  
674 Yale, 2003; Reiter et al., 2024).

675 The 1 km spatial distance limit can also be confirmed by viewing the  $S_{H\max}$  orientation from the boreholes in  
676 correlation with their distance from the nearest faults. The TRU1-1 borehole is less than 1 km from the  
677 Neuhausen fault. Similarly, the MAR1-1 and RHE1-1 boreholes are closest to the Rheinau fault. The average  $S_{H\max}$   
678 orientation from the BO, DITF, and HF is  $\sim 165^\circ$  along the TRU1-1 borehole,  $\sim 175^\circ$  along the MAR1-1 borehole,  
679 and  $\sim 172.5^\circ$  along the RHE1-1 borehole (Nagra, 2024c, d). Comparing the  $S_{H\max}$  orientation values from these  
680 three boreholes to the regional  $S_{H\max}$  orientation value of  $170^\circ \pm 11^\circ$  already strengthens the argument that the  
681 faults have minimal effects on  $S_{H\max}$  orientation even at a distance of less than 1 km.

682 (Bell, 1996a; Yale, 2003; Reiter et al., 2024)

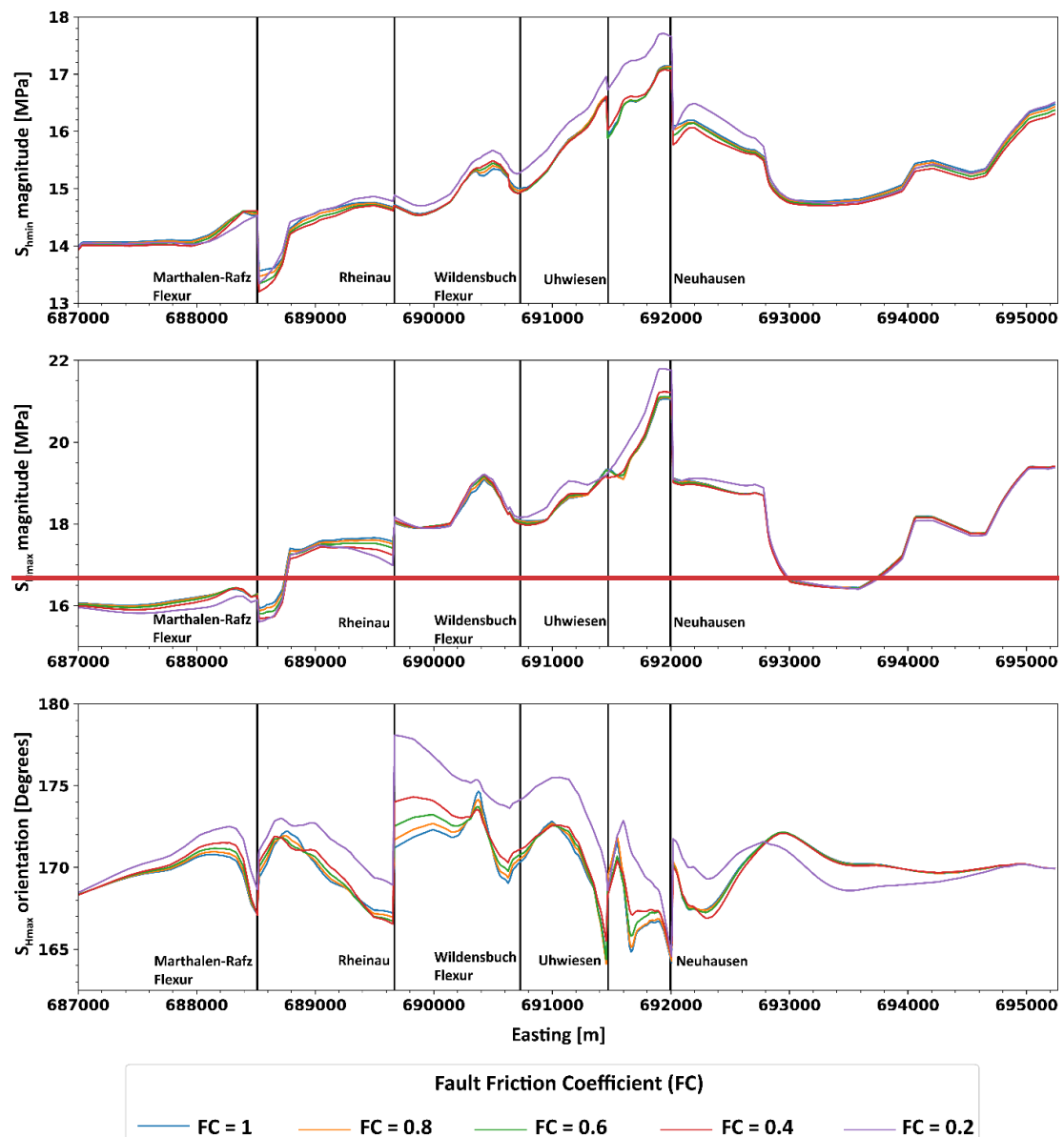
## 683 5.2 Impact of varying fault friction coefficient of the implemented faults

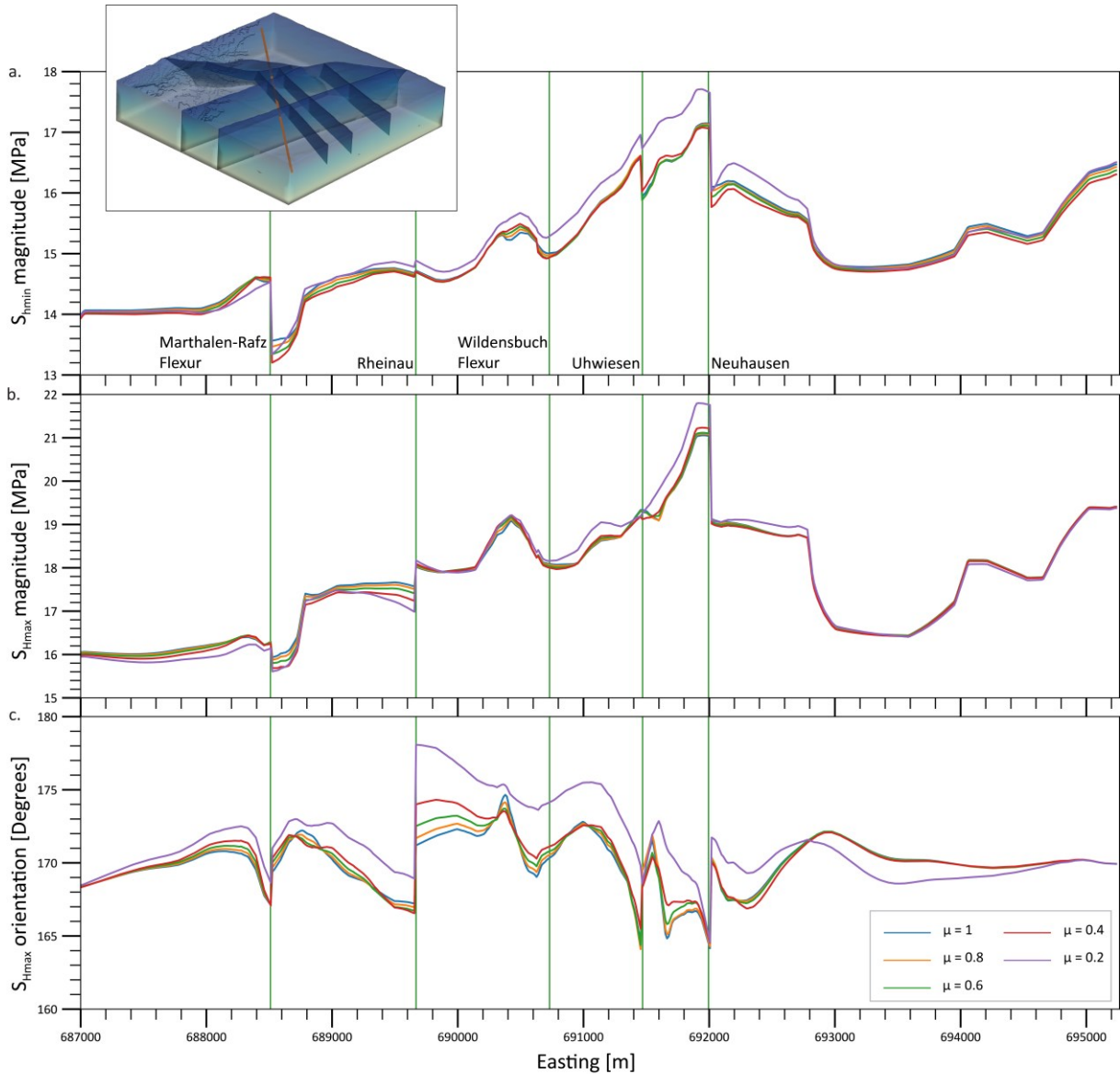
684 In geomechanical modelling, the fault strength is commonly describedbyMohrCoulombcriteriaandhence  
685 characterized by its friction coefficient ( $\mu$ ) and cohesion (Brandes and Tanner, 2020). In most geological settings,  
686 the friction coefficient varies between 0.6 and 1.0 in reservoirs with depths where normalstressesare<200  
687 MPa on a pre-existing fracture plane (Byerlee, 1978; Zoback and Healy, 1984). In stark contrast, significantly  
688 lower friction coefficient values are found in geological settings with extremely weak lithologies, overpressured  
689 fault cores, and in faults with very large offset and/or high slip rates (Morrow et al., 1982; Morrow et al., 1992;  
690 Di Toro et al., 2011; Hergert et al., 2011; Li et al., 2022). Cohesion varies with different lithologies, but for the  
691 pre-existing faults, it is commonly assumed to be zero. In general, the value of the friction coefficient values  
692 varies between 0.4 and 0.8, and is standardly taken as 0.65 (Hawkes et al., 2005; Kohli and Zoback, 2013). In  
693 northern Switzerland, taking the lithology and the geological setting into consideration, the values of apparent  
694 fault friction coefficient alsovaluescommonly range from 0.6 to 1.0, and very rarely to 0.4 (Kastrup, 2002; Viganò  
695 et al., 2021). Asseeninthestudiesby Kastrup (2002), statesthatthe apparent fault friction values of 0.2 areis  
696 extremely rare in the Switzerland and only occurs at depths of more than 10 km.

697 We investigate the effect of varying the friction coefficient of the contact surfaces on the predicted in situ stress  
698 state and re-calibrating the REF each model with a different friction coefficient seperately. Weconsiderallthe  
699 realisticallypossiblevaluesoffrictioncoefficientinSwitzerlandbutitmustbekeptinmindthatthefriction  
700 coefficientvaluesbelow0.6werecategorizedas'anomalous'inSwitzerland(Kastrup, 2002). The results of stress  
701 magnitudes and orientation from friction coefficients 0.2, 0.4, 0.6, and 0.8 are compared to the friction  
702 coefficient of 1.0, the value we use in the REF model (Fig. 11). We see that changes in friction coefficient do not  
703 significantly affect our model results beyond lateral distances of 1 km. Even within 1 km from the faults, boththe  
704 horizontal stress magnitudes have observable variations of  $<1$  MPa and  $<5^\circ$  for the  $S_{H\max}$  orientation variations.  
705 These variations reduce to  $<0.25$  MPa in both minimum and maximum horizontal stresses, and  $<2.5^\circ$  in the  $S_{H\max}$   
706 orientation beyond 1 km from the faults. The maximum variations, still far less than the uncertainties in the  
707 measurementsinsitustressdata of the stress magnitudes and resolvable  $S_{H\max}$  orientations, occur at a friction

708 coefficient of 0.2. For the other values of the friction coefficient, the results are very much comparable to the  
709 REF mModel, with a friction coefficient of 1. This is to show that changing the friction coefficient has a negligible  
710 effect on the predicted stresses in our model. but might not be the case in other studies. Minor amounts of slip,  
711 in the order of a few tens of cm, occur along the faults in the REF model during the application of boundary  
712 conditions. However, the stress change along the fault due to this slip is expected to be far less than the much  
713 larger background stresses and the differential stresses. Therefore, the minor slip occurring along the contact  
714 surfaces does not influence the overall stress field analysis.

715 These findings are in line with the results from the generic studies by Homberg et al. (1997) and Reiter et al.  
716 (2024), who studied the impact of variable friction coefficient on adifferent stress tensorcomponents and found  
717 that lower values of friction coefficient lead to a higher stress perturbation near the modelled fault. This is also  
718 seen in Fig. 11 and is because of possible decoupling at the fault and consequently a better dissipation of stress  
719 at the faults, facilitated by lower friction coefficients. The studies also showed that this effect is limited to a  
720 distance of 1 km from the fault zone.





722  
723 **Figure 11: Impact of friction coefficient ( $\mu$ ) on the stress tensor components. The model used here is the REF model. The**  
724 **results are plotted along the SW-NE horizontal profile at 300 m (b.s.l.), shown in the 3D figure as a red line. Green vertical**  
725 **lines with the respective fault names denote the location where the profile crosses the modelled faults.**

726 **Impact of friction coefficient on the stress tensor components. The lower the friction coefficient, the larger the stress**  
727 **perturbations near the faults. The results are plotted along the same horizontal line profile at the depth of -300 bsl, as used**  
728 **in Fig. 10. The stress perturbations increase with decrease in friction coefficient values but their effect is observable only**  
729 **within  $\sim 1$  km from the modelled faults. Given that the average width of the  $S_{\text{min}}$  and  $S_{\text{max}}$  ranges are 0.7 MPa and 3.5 MPa**  
730 **respectively, the differences seen above are negligible.**

731 5.3 Dependence of the modeling results on fault implementation

732 Faults in the REF model are represented as contact surfaces, a common and effective approach for large-scale  
733 geomechanical simulations. Using contact elements to model faults seems to be a reasonable simplification for  
734 large, field-scale reservoir models, where the actual width of the fault core is much smaller than the overall size  
735 of the model. Hence, contact surfaces are computationally efficient for reservoir-scale models where actual fault  
736 zone widths are negligible compared to model dimensions (Caine et al., 1996; Treffeisen and Henk, 2020). Since  
737 our interest is on reservoir scale, alternative fault representation using, e.g. continuous rectangular finite  
738 element grid, or a continuous curvilinear finite element grid in a homogenized continuum (Henk, 2009, 2020) are  
739 not used in our study. Furthermore, the results from Treffeisen and Henk (2020) and Reiter et al. (2024) show  
740 that the stress and strain perturbations from different technical fault implementations vary only within a few  
741 tens to a few hundred meters from the fault representation. As we focus only on the far-field stress state, it can

742 be safely assumed that the choice of fault implementation approach does not significantly affect the far-field  
743 results.

744 Although a numerical value does not exist for what is universally defined as far-field stresses, our model indicates  
745 that at a distance of >500 m from the faults, the impact of the faults on the stress field is clearly smaller than  
746 the uncertainty of the model itself and smaller than the expected variability of the stress field (Nagra, 2024).  
747 As seen in Fig. 910, the influence of faults on the stress field is limited to within 1 km from the contact surfaces.  
748 Beyond this distance, the choice of the fault representation approach would not have no significant impact on  
749 the predicted in situ stress state.

## 750 5.4 Limitations of the study's results and future outlook

751 In the REF model, the faults, represented by contact surfaces, are simplified and a unified representation of  
752 numerous small fault patches that were interpreted from the 3D seismic interpretation. This simplification is  
753 necessary for an easier and reasonable representation of fault structures and the consequent computational  
754 simulation feasibility of the model. However, the reality is more complex. In the subsurface, faults often occur in  
755 clusters and display heterogeneous geometry, composition, and structure (Tanner and Brandes, 2020). Large  
756 faults are often accompanied by zones of secondary faults, which can extend the spatial influence of faults on  
757 the stress state. Small fault segments of the primary fault and the associated secondary faults can lead to a higher  
758 stress concentration along the fault surfaces, complicating the interaction between faults and the in situ stresses  
759 (Jones, 1988; Maerten et al., 2002). A single fault may also have complex geometry with multiple bends (Saucier  
760 et al., 1992; Roche et al., 2021), increasing its influence on stresses compared to the planar faults.

761 Our study focuses on a reservoir scale, in the order of a few km<sup>2</sup>, to predict present-day stress variation in the  
762 area of interest. While seven faults were implemented in the REF model, many more fractures or joints exist in  
763 reality but cannot be resolved at our current lateral resolution of approximately 70–100 m, and the available  
764 structural geological data. Including these would significantly increase the element count and computational  
765 demand, far beyond the scope or need of most studies. It is important to emphasize that the focus of our the  
766 results is only the far-field present day stresses, and in an intact and undisturbed rock volume.

767 While previous studies (Homberg et al., 1997; Nicol et al., 2020) have documented significant stress rotations  
768 near fault tips, they also emphasize that these perturbations are typically localized, rarely extending beyond a  
769 few hundred meters from the termination point (Homberg et al., 1997; Nicol et al., 2020). Our findings are in  
770 general agreement with this observation. In our model, fault tips ending within the Mesozoic sediments indeed  
771 exhibit localized stress concentrations and enhanced stress rotations. However, because these effects are  
772 spatially restricted, they do not significantly alter the regional stress field predicted by the fault-agnostic models  
773 at distances greater than a few 100 m from the structural discontinuities.

774 Furthermore, extreme Extreme cases exist where large-scale faulting separated the crust into distinct fault blocks,  
775 each having an independent  $S_{H\max}$  orientation between adjacent fault blocks of the same field (Yale et al., 1994;  
776 Yale and Ryan, 1994; Bell, 1996b; Kattenhorn et al., 2000; Hergert and Heidbach, 2011; Hergert et al., 2011; Li et  
777 al., 2019; Qin et al., 2024). While complex stress patterns and large  $S_{H\max}$  rotations have been reported for major  
778 fault systems such as the Møre–Trøndelag Fault Complex and the San Andreas Fault, these systems differ  
779 fundamentally from the Alpine Foreland Basin in terms of tectonic setting, fault displacement magnitude, and  
780 fault frictional properties (Zoback et al., 1987; Pascal and Gabrielsen, 2001; Roberts and Myrvang, 2004). In  
781 particular, the large offsets and anomalously low friction coefficients reported for these systems are not  
782 representative of the fault conditions in northern Switzerland. (Zoback et al., 1987; Pascal and Gabrielsen, 2001;  
783 Roberts and Myrvang, 2004) But But, as seen in our study area region, if the Mesozoic sediments are not massively  
784 faulted or fractured, and have sufficiently large differential stresses, and are located in an intraplate Foreland  
785 Basin setting, it could be expected that the impact of faults on the stress state would only be within 1 km from  
786 the fault zone. However, further investigation is needed for other geological settings, with different lithologies  
787 such as salt domes, anhydrite, or crystalline rock formations, or regions where faults exhibit more complex  
788 geometry with more curvature/ bends, or with extremely large total offsets and high slip rates, to confirm the  
789 broader applicability of our results.

790 6. Conclusion

791 We evaluated the influence of faults on the regional stress state using 3D geomechanical models of the Zürich  
792 Nordost siting region, which are calibrated on a robust dataset of 30 minimum horizontal and 15 maximum  
793 horizontal stress magnitudes from two boreholes. We directly compare the predicted stress states between  
794 models where faults have been modelled as contact surfaces and models where faults have been excluded or  
795 mechanically deactivated. Our findings show that faults cause only local stress perturbations, within 500 m from  
796 the contact surfaces, with their impact becoming negligible beyond 1 km from the fault-~~core~~. At this scale, stress  
797 variations are mainly controlled by contrasts in rock stiffness on the juxtaposed formations rather than just the  
798 relative mechanical weakness presented by the fault plane. The variations between the model realizations must  
799 also be viewed in conjunction with the rock stress variability, which in turn results from stiffness variability. The  
800 fault-induced stress effects at distances  $>1$  km are smaller than the typical resolution limits of stress data and  
801 uncertainties of the stress magnitude measurements, which ~~is-are~~  $\pm 151^\circ$  for  $S_{H\max}$  orientation and 0.7–3.5 MPa  
802 for stress magnitude, derived from the description of stress magnitudes as ranges. Importantly, omitting faults  
803 from the modeling workflow can reduce model-~~setup~~ and computational time from months to 1–2 days using  
804 alternative discretization strategies, without sacrificing stress prediction reliability~~accuracy~~. These findings  
805 provide valuable guidance for efficient and reliable reservoir-scale geomechanical modeling, including ~~repository~~  
806 site assessments for a deep geological repository, where predicting far-field in situ stresses in intact rock volumes  
807 is essential, given that the storage sites are located away from active faults ( $>1$  km) in an intact and undisturbed  
808 rock volume. However, further studies in different geologic settings and under different stress conditions are  
809 required to verify the general applicability of our results from northern Switzerland.

810 Author ~~E~~contribution

811 LSARV: Conceptualization, Formal analysis, Methodology, Model preparation, Validation, Visualization, Writing  
812 (original draft preparation), and Writing (review and editing).

813 OH: Conceptualization, Data curation, Funding acquisition, Project administration, Resources, Supervision,  
814 Validation, and Writing (review and editing).

815 MZ: Resources, Software, Supervision, Validation, and Writing (review and editing).

816 KR: Methodology, Resources, Model preparation, Validation, and Writing (review and editing), Funding  
817 acquisition.

818 AH: Funding acquisition, Project administration, and Writing (review and editing).

819 MR: Conceptualization, Visualization, Writing (review and editing).

820 SBG: Resources, and Writing (review and editing).

821 TH: Visualization, Writing (review and editing).

822 Competing Interests

823 The authors declare that they have no conflict of interest.

824 Disclaimer

825 Publisher's note: Copernicus Publications remains neutral with regard to jurisdictional claims made in the text,  
826 published maps, institutional affiliations, or any other geographical representation in this paper. While  
827 Copernicus Publications makes every effort to include appropriate place names, the final responsibility lies with  
828 the authors.

829 Acknowledgements

830 We thank NAGRA for providing access to the extensive dataset used in our study. We also thank SQuaRe and  
831 SpannEnd 2.0 for the funding.

832 Financial ~~s~~Support

833 The authors gratefully acknowledge the funding provided by the Bundesministerium für Umwelt, Naturschutz,  
834 nukleare Sicherheit und Verbraucherschutz through the project SQuaRe (project number: 02E12062B), and by  
835 the Bundesgesellschaft für Endlagerung (BGE) through the project SpannEnD 2.0 (<https://www.spannend-projekt.de>). Additional support was provided by the National Cooperative for the Disposal of Radioactive Waste  
836 (Nagra), Switzerland.

838 References

839 Ahlers, S., Henk, A., Hergert, T., Reiter, K., Müller, B., Röckel, L., Heidbach, O., Morawietz, S., Scheck-  
840 Wenderoth, M., and Anikiev, D.: 3D crustal stress state of Germany according to a data-calibrated geomechanical  
841 model, *Solid Earth*, 12, 1777–1799, <https://doi.org/10.5194/se-12-1777-2021>, 2021.

842 Ahlers, S., Röckel, L., Hergert, T., Reiter, K., Heidbach, O., Henk, A., Müller, B., Morawietz, S., Scheck-  
843 Wenderoth, M., and Anikiev, D.: The crustal stress field of Germany: a refined prediction, *Geothermal Energy*,  
844 10, 10, <https://doi.org/10.1186/s40517-022-00222-6>, 2022.

845 Aleksandrowski, P., Inderhaug, O. H. E., and Knapstad, B.: Tectonic structures and wellbore breakout orientation,  
846 The 33rd U.S. Symposium on Rock Mechanics (USRMS), Santa Fe, New Mexico, USA, 3–5 June,  
847 [https://doi.org/10.1016/0148-9062\(93\)90652-T](https://doi.org/10.1016/0148-9062(93)90652-T), 1992.

848 Amadei, B. and Stephansson, O.: Rock stress and its measurement, Springer Dordrecht,  
849 <https://doi.org/10.1007/978-94-011-5346-1>, 1997.

850 Azzola, J., Valley, B., Schmittbuhl, J., and Genter, A.: Stress characterization and temporal evolution of borehole  
851 failure at the Rittershoffen geothermal project, *Solid Earth*, 10, 1155–1180, <https://doi.org/10.5194/se-10-1155-2019>, 2019.

853 Barton, C. A. and Zoback, M. D.: Stress perturbations associated with active faults penetrated by boreholes:  
854 Possible evidence for near-complete stress drop and a new technique for stress magnitude measurement, *Journal  
855 of Geophysical Research: Solid Earth*, 99, 9373–9390, <https://doi.org/10.1029/93JB03359>, 1994.

856 Bell, J. S.: Petro Geoscience 1. In situ stresses in sedimentary rocks (Part 1): Measurement Techniques, *Geoscience  
857 Canada*, 23, 1996a.

858 Bell, J. S.: Petro Geoscience 2. In-Situ Stresses in Sedimentary Rocks (Part 2): Application of Stress  
859 Measurements, *Geoscience Canada*, 23, 135–153, 1996b.

860 Bell, J. S. and Gough, D. I.: Northeast-southwest compressive stress in Alberta evidence from oil wells, *Earth and  
861 Planetary Science Letters*, 45, 475–482, [https://doi.org/10.1016/0012-821X\(79\)90146-8](https://doi.org/10.1016/0012-821X(79)90146-8), 1979.

862 Bell, J. S. and Grasby, S. E.: The stress regime of the Western Canadian Sedimentary Basin, *Geofluids*, 12, 150–  
863 165, <https://doi.org/10.1111/j.1468-8123.2011.00349.x>, 2012.

864 Bérard, T. and Desroches, J.: Geological structure, geomechanical perturbations, and variability in hydraulic  
865 fracturing performance at the scale of a square mile, *Geomechanics for Energy and the Environment*, 26, 100137,  
866 <https://doi.org/10.1016/j.gete.2019.100137>, 2021.

867 Berard, T., Sinha, B. K., Van Ruth, P., Dance, T., John, Z., and Tan, C.: Stress estimation at the Otway CO<sub>2</sub>  
868 storage site, Australia, *SPE Asia Pacific Oil and Gas Conference and Exhibition*, Perth, Australia,  
869 <https://doi.org/10.2118/116422-MS>, 2008.

870 Boness, N. L. and Zoback, M. D.: A multiscale study of the mechanisms controlling shear velocity anisotropy in  
871 the San Andreas Fault Observatory at Depth, *GEOPHYSICS*, 71, F131–F146, <https://doi.org/10.1190/1.2231107>,  
872 2006.

873 Brandes, C. and Tanner, D. C.: Chapter 2 - Fault mechanics and earthquakes, in: *Understanding Faults*, edited by:  
874 Tanner, D., and Brandes, C., Elsevier, 11–80, <https://doi.org/10.1016/B978-0-12-815985-9.00002-3>, 2020.

875 Brodsky, E. E., Mori, J. J., Anderson, L., Chester, F. M., Conin, M., Dunham, E. M., Eguchi, N., Fulton, P. M.,  
876 Hino, R., Hirose, T., Ikari, M. J., Ishikawa, T., Jeppson, T., Kano, Y., Kirkpatrick, J., Kodaira, S., Lin, W.,  
877 Nakamura, Y., Rabinowitz, H. S., Regalla, C., Remitti, F., Rowe, C., Saffer, D. M., Saito, S., Sample, J., Sanada,  
878 Y., Savage, H. M., Sun, T., Toczko, S., Ujiie, K., Wolfson-Schwehr, M., and Yang, T.: The State of Stress on the  
879 Fault Before, During, and After a Major Earthquake, *Annual Review of Earth and Planetary Sciences*, 48, 49–74,  
880 <https://doi.org/10.1146/annurev-earth-053018-060507>, 2020.

881 Brooke-Barnett, S., Flottmann, T., Paul, P. K., Busetti, S., Hennings, P., Reid, R., and Rosenbaum, G.: Influence  
882 of basement structures on in situ stresses over the Surat Basin, southeast Queensland, *Journal of Geophysical  
883 Research: Solid Earth*, 120, 4946–4965, <https://doi.org/10.1002/2015JB011964>, 2015.

884 Brudy, M., Fuchs, K., and Zoback, M. D.: Stress orientation profile to 6 km depth in the KTB main borehole, KTB  
885 Report 93-2: Contributions to the 6. Annual KTB-Colloquium, *Geoscientific Results*, Giessen, Germany, 1–2 June,  
886 195–197, <https://doi.org/10.2312/KTB.93-2>, 1992.

887 Brudy, M., Zoback, M. D., Fuchs, K., Rummel, F., and Baumgärtner, J.: Estimation of the complete stress tensor  
888 to 8 km depth in the KTB scientific drill holes: Implications for crustal strength, *Journal of Geophysical Research: Solid  
889 Earth*, 102, 18453–18475, <https://doi.org/10.1029/96JB02942>, 1997.

890 Buchmann, T. J. and Connolly, P. T.: Contemporary kinematics of the Upper Rhine Graben: A 3D finite element  
891 approach, *Global and Planetary Change*, 58, 287–309, <https://doi.org/10.1016/j.gloplacha.2007.02.012>, 2007.

892 Burkhard, M. and Sommaruga, S.: Evolution of the western Swiss Molasse basin: structural relations with the Alps  
893 and the Jura belt, *Geological Society, London, Special Publications*, 134, 279–298,  
894 <https://doi.org/10.1144/GSL.SP.1998.134.01.13>, 1998.

895 Byerlee, J.: Friction of rocks, *pure and applied geophysics*, 116, 615–626, <https://doi.org/10.1007/BF00876528>,  
896 1978.

897 Caine, J. S., Evans, J. P., and Forster, C. B.: Fault zone architecture and permeability structure, *Geology*, 24, 1025–  
898 1028, [https://doi.org/10.1130/0091-7613\(1996\)024%3C1025:FZAAPS%3E2.3.CO;2](https://doi.org/10.1130/0091-7613(1996)024%3C1025:FZAAPS%3E2.3.CO;2), 1996.

899 Catalli, F., Meier, M.-A., and Wiemer, S.: The role of Coulomb stress changes for injection-induced seismicity:  
900 The Basel enhanced geothermal system, *Geophysical Research Letters*, 40, 72–77,  
901 <https://doi.org/10.1029/2012GL054147>, 2013.

902 Chéry, J., Zoback, M. D., and Hickman, S.: A mechanical model of the San Andreas fault and SAFOD Pilot Hole  
903 stress measurements, *Geophysical Research Letters*, 31, <https://doi.org/10.1029/2004GL019521>, 2004.

904 Cloetingh, S., Cornu, T., Ziegler, P. A., and Beekman, F.: Neotectonics and intraplate continental topography of  
905 the northern Alpine Foreland, *Earth-Science Reviews*, 74, 127–196,  
906 <https://doi.org/10.1016/j.earscirev.2005.06.001>, 2006.

907 Cloetingh, S. and Wortel, R.: Regional stress field of the Indian Plate, *Geophysical Research Letters*, 12, 77–80,  
908 <https://doi.org/10.1029/GL012i002p00077>, 1985.

909 Coward, M. and Dietrich, D.: Alpine tectonics — an overview, *Geological Society, London, Special Publications*,  
910 45, 1–29, <https://doi.org/10.1144/GSL.SP.1989.045.01.0>, 1989.

911 Desroches, J., Peyret, E., Gisolf, A., Wilcox, A., Di Giovann'i, M., de Jong, A. S., Sepehri, S., Garrard, R., and  
912 Giger, S.: Stress Measurement Campaign in Scientific Deep Boreholes: Focus on Tools and Methods, *Petrophysics  
913 - The SPWLA Journal*, 64, 621–639, <https://doi.org/10.30632/PJV64N5-2023a2>, 2023.

914 Desroches, J., Peyret, E., Gisolf, A., Wilcox, A., Di Giovanni, M., de Jong, A. S., Sepehri, S., Garrard, R., and  
915 Giger, S.: Stress Measurement Campaign in Scientific Deep Boreholes: Focus on Tool and Methods, SPWLA  
916 62nd Annual Logging Symposium, Virtual Event, 17–20 May, <https://doi.org/10.30632/SPWLA-2021-0056>,  
917 2021a.

918 Desroches, J., Peyret, E., Gisolf, A., Wilcox, A., Di Giovanni, M., Schram de Jong, A., Milos, B., Gonus, J.,  
919 Bailey, E., Sepehri, S., Garitte, B., Garrard, R., and Giger, S.: Stress-Measurement Campaign in Scientific Deep  
920 Boreholes: From Planning to Interpretation, 55th U.S. Rock Mechanics/Geomechanics Symposium, Virtual Event,  
921 20–23 June, 2021b.

922 Di Toro, G., Han, R., Hirose, T., De Paola, N., Nielsen, S., Mizoguchi, K., Ferri, F., Cocco, M., and Shimamoto,  
923 T.: Fault lubrication during earthquakes, *Nature*, 471, 494–498, <https://doi.org/10.1038/nature09838>, 2011.

924 Diebold, P. and Noack, T.: Late Palaeozoic troughs and Tertiary structures in the eastern Folded Jura, in: Deep  
925 Structure of the Swiss Alps: Results of NRP20, edited by: Pfiffner, O. A., Lehner, P., Heitzmann, P., Mueller, S.,  
926 and Steck, A., Birkhäuser Verlag, Basel, 59–63, 1997.

927 Fiebig, M. and Preusser, F.: Pleistocene glaciations of the northern Alpine Foreland, *Geographica Helvetica*, 63,  
928 145–150, <https://doi.org/10.5194/gh-63-145-2008>, 2008.

929 Fischer, K. and Henk, A.: A workflow for building and calibrating 3-D geomechanical models- a case study for a  
930 gas reservoir in the North German Basin, *Solid Earth*, 4, 347–355, <https://doi.org/10.5194/se-4-347-2013>, 2013.

931 Gens, A., Garitte, B., Olivella, S., and Vaunat, J.: Applications of multiphysical geomechanics in underground  
932 nuclear waste storage, *European Journal of Environmental and Civil Engineering*, 13, 7–8,  
933 <https://doi.org/10.1080/19648189.2009.9693162>, 2009.

934 Gorin, G., Signer, C., and Amberger, G.: Structural configuration of the western Swiss Molasse Basin as defined  
935 by reflection seismic data, *Eclogae Geologicae Helvetiae*, 86, 693–716, 1993.

936 Gough, D. I. and Bell, J. S.: Stress orientations from borehole wall fractures with examples from Colorado, east  
937 Texas, and northern Canada, *Canadian Journal of Earth Sciences*, 19, 1358–1370, <https://doi.org/10.1139/e82-118>,  
938 1982.

939 Hawkes, C., McLellan, P., and Bachu, S.: Geomechanical factors affecting geological storage of CO<sub>2</sub> in depleted  
940 oil and gas reservoirs, *Journal of Canadian Petroleum Technology*, 44, 2005.

941 Heidbach, O., Rajabi, M., Cui, X., Fuchs, K., Müller, B., Reinecker, J., Reiter, K., Tingay, M., Wenzel, F., Xie,  
942 F., Ziegler, M. O., Zoback, M.-L., and Zoback, M.: The World Stress Map database release 2016: Crustal stress  
943 pattern across scales, *Tectonophysics*, 744, 484–498, <https://doi.org/10.1016/j.tecto.2018.07.007>, 2018.

944 Heidbach, O., Rajabi, M., Di Giacomo, D., Harris, J., Lammers, S., Morawietz, S., Pierdominici, S., Reiter, K.,  
945 Storchak, D., von Specht, S., and Ziegler, M. O.: World Stress Map Database Release 2025,  
946 <https://doi.org/10.5880/WSM.2025.001>, 2025a.

947 Heidbach, O., Reinecker, J., Diehl, T., Desroches, J., Ziegler, M. O., Reiter, K., Vietor, T., and Giger, S. B.: The  
948 present-day crustal stress field of the Molasse Basin in Switzerland, *Swiss Journal of Geosciences*,  
949 <https://doi.org/10.1186/s00015-025-00487-6>, 2025b.

950 Heidbach, O., Reinecker, J., Tingay, M., Müller, B., Sperner, B., Fuchs, K., and Wenzel, F.: Plate boundary forces  
951 are not enough: Second- and third-order stress patterns highlighted in the World Stress Map database, *Tectonics*,  
952 26, TC6014, <https://doi.org/10.1029/2007TC002133>, 2007.

953 Henk, A.: Pre-drilling prediction of the tectonic stress field with geomechanical models, *First Break*, 23, 53–57,  
954 <https://doi.org/10.3997/1365-2397.2005021>, 2005.

955 Henk, A.: Perspectives of Geomechanical Reservoir Models - Why Stress is Important, *Oil Gas European  
956 Magazine*, 35(1), 20–24, 2009.

957 Henk, A.: Chapter 4 - Numerical modelling of faults, in: *Understanding Faults*, edited by: Tanner, D., and Brandes,  
958 C., Elsevier, 147–165, <https://doi.org/10.1016/B978-0-12-815985-9.00004-7>, 2020.

959 Hergert, T. and Heidbach, O.: Geomechanical model of the Marmara Sea region—II. 3-D contemporary  
960 background stress field, *Geophysical Journal International*, 185, 1090–1102, <https://doi.org/10.1111/j.1365-246X.2011.04992.x>, 2011.

962 Hergert, T., Heidbach, O., Bécel, A., and Laigle, M.: Geomechanical model of the Marmara Sea region - I. 3-D  
963 contemporary kinematics, *Geophysical Journal International*, 185, 1073–1089, <https://doi.org/10.1111/j.1365-246X.2011.04991.x>, 2011.

965 Hergert, T., Heidbach, O., Reiter, K., Giger, S. B., and Marschall, P.: Stress field sensitivity analysis in a  
966 sedimentary sequence of the Alpine foreland, northern Switzerland, *Solid Earth*, 6, 533–552,  
967 <https://doi.org/10.5194/se-6-533-2015>, 2015.

968 Hickman, S. and Zoback, M.: Stress orientations and magnitudes in the SAFOD pilot hole, *Geophysical Research  
969 Letters*, 31, <https://doi.org/10.1029/2004GL020043>, 2004.

970 Homberg, C., Hu, J. C., Angelier, J., Bergerat, F., and Lacombe, O.: Characterization of stress perturbations near  
971 major fault zones: insights from 2-D distinct-element numerical modelling and field studies (Jura mountains),  
972 *Journal of Structural Geology*, 19, 703–718, [https://doi.org/10.1016/S0191-8141\(96\)00104-6](https://doi.org/10.1016/S0191-8141(96)00104-6), 1997.

973 Illies, J. H.: The Rhine graben rift system-plate tectonics and transform faulting, *Geophysical surveys*, 1, 27–60,  
974 <https://doi.org/10.1007/BF01449550>, 1972.

975 Jaeger, J. C., Cook, N. G. W., and Zimmerman, R. W.: *Fundamentals of Rock Mechanics*, 4, Blackwell Publishing,  
976 2007.

977 Jo, Y., Chang, C., Ji, S.-H., and Park, K.-W.: In situ stress states at KURT, an underground research laboratory in  
978 South Korea for the study of high-level radioactive waste disposal, *Engineering Geology*, 259, 105198,  
979 <https://doi.org/10.1016/j.enggeo.2019.105198>, 2019.

980 Jones, W. B.: Listric growth faults in the Kenya Rift Valley, *Journal of Structural Geology*, 10, 661–672,  
981 [https://doi.org/10.1016/0191-8141\(88\)90074-0](https://doi.org/10.1016/0191-8141(88)90074-0), 1988.

982 Jordan, P.: Triassic. Basin evolution: Switzerland., in: *The Geology of Central Europe. Volume 2: Mesozoic and  
983 Cenozoic*, edited by: McCann, T., Geological Society of London, London, 785–788,  
984 <https://doi.org/10.1144/CEV2P>, 2008.

985 Kastrup, U.: Seismotectonics and Stress Field Variations in Switzerland, Dissertation, Swiss Federal Institute of  
986 Technology Zurich (ETH Zurich), Zurich, 162 pp., <https://doi.org/10.3929/ethz-a-004423062>, 2002.

987 Kattenhorn, S. A., Aydin, A., and Pollard, D. D.: Joints at high angles to normal fault strike: an explanation using  
988 3-D numerical models of fault-perturbed stress fields, *Journal of Structural Geology*, 22, 1–23,  
989 [https://doi.org/10.1016/S0191-8141\(99\)00130-3](https://doi.org/10.1016/S0191-8141(99)00130-3), 2000.

990 Kempf, O. and Adrian, P., O.: Early Tertiary evolution of the North Alpine Foreland Basin of the Swiss Alps and  
991 adjoining areas, *Basin Research*, 16, 549–567, <https://doi.org/10.1111/j.1365-2117.2004.00246.x>, 2004.

992 Kingsborough, R. H., Williams, A. F., and Hillis, R. R.: Borehole Instability on the Northwest Shelf of Australia,  
993 SPE Asia-Pacific Conference, Perth, Australia, 4–7 Nov, <https://doi.org/10.2118/23015-MS>, 1991.

994 Kohli, A. H. and Zoback, M. D.: Frictional properties of shale reservoir rocks, *Journal of Geophysical Research:  
995 Solid Earth*, 118, 5109–5125, <https://doi.org/10.1002/jgrb.50346>, 2013.

996 Laubscher, H.: Jura, Alps and the boundary of the Adria subplate, *Tectonophysics*, 483, 223–239,  
997 <https://doi.org/10.1016/j.tecto.2009.10.011>, 2010.

998 Lecampion, B. and Lei, T.: Reconstructing the 3D Initial Stress State over Reservoir Geomechanics Model from  
999 Local Measurements and Geological Priors: A Bayesian Approach, *Schlumberger J. of Modeling, Design and  
1000 Simulation*, 1, 100–104, <https://infoscience.epfl.ch/handle/20.500.14299/119734>, 2010.

1001 Li, P., Cai, M.-f., Miao, S.-j., and Guo, Q.-f.: New Insights Into The Current Stress Field Around the Yishu Fault  
 1002 Zone, Eastern China, *Rock Mechanics and Rock Engineering*, 52, 4133–4145, <https://doi.org/10.1007/s00603-019-01792-x>, 2019.

1004 Li, X., Hergert, T., Henk, A., and Zeng, Z.: Contemporary background stress field in the eastern Tibetan Plateau:  
 1005 Insights from 3D geomechanical modeling, *Tectonophysics*, 822, 229177,  
 1006 <https://doi.org/10.1016/j.tecto.2021.229177>, 2022.

1007 Long, J. C. S. and Ewing, R. C.: YUCCA MOUNTAIN: Earth-Science Issues at a Geologic Repository for High-  
 1008 Level Nuclear Waste, *Annual Review of Earth and Planetary Sciences*, 32, 363–401,  
 1009 <https://doi.org/10.1146/annurev.earth.32.092203.122444>, 2004.

1010 Madritsch, H., Looser, N., Schneeberger, R., Wohlwend, S., Guillong, M., and Malz, A.: Reconstructing the  
 1011 Evolution of Foreland Fold-And-Thrust Belts Using U-Pb Calcite Dating: An Integrated Case-Study From the  
 1012 Easternmost Jura Mountains (Switzerland), *Tectonics*, 43, e2023TC008181,  
 1013 <https://doi.org/10.1029/2023TC008181>, 2024.

1014 Maerten, L., Gillespie, P., and Pollard, D. D.: Effects of local stress perturbation on secondary fault development,  
 1015 *Journal of Structural Geology*, 24, 145–153, [https://doi.org/10.1016/S0191-8141\(01\)00054-2](https://doi.org/10.1016/S0191-8141(01)00054-2), 2002.

1016 Mao, J.: A finite element approach to solve contact problems in geotechnical engineering, *International Journal  
 1017 for Numerical and Analytical Methods in Geomechanics*, 29, 525–550, <https://doi.org/10.1002/nag.424>, 2005.

1018 Marchant, R., Ringgenberg, Y., Stampfli, G., Birkhäuser, P., Roth, P., and Meier, B.: Paleotectonic evolution of  
 1019 the Zürcher Weinland (northern Switzerland), based on 2D and 3D seismic data, *Eclogae Geologicae Helvetiae*,  
 1020 98, 345–362, <https://doi.org/10.1007/s00015-005-1171-8>, 2005.

1021 McCann, T., Pascal, C., Timmerman, M. J., Krzywiec, P., López-Gómez, J., Wetzel, L., Krawczyk, C. M., Rieke,  
 1022 H., and Lamarche, J.: Post-Variscan (end Carboniferous-Early Permian) basin evolution in Western and Central  
 1023 Europe, *Geological Society, London, Memoirs*, 32, 355–388, <https://doi.org/10.1144/GSL.MEM.2006.032.01.22>,  
 1024 2006.

1025 Morrow, C., Radney, B., and Byerlee, J.: Chapter 3 Frictional Strength and the Effective Pressure Law of  
 1026 Montmorillonite and Illite Clays, in: *International Geophysics*, edited by: Evans, B., and Wong, T.-f., Academic  
 1027 Press, 69–88, [https://doi.org/10.1016/S0074-6142\(08\)62815-6](https://doi.org/10.1016/S0074-6142(08)62815-6), 1992.

1028 Morrow, C., Shi, L., and Byerlee, J.: Strain hardening and strength of clay-rich fault gouges, *Journal of  
 1029 Geophysical Research: Solid Earth*, 87, 6771–6780, <https://doi.org/10.1029/JB087iB08p06771>, 1982.

1030 Nagra: Erläuterungen zur Geologischen Karte der zentralen Nordschweiz 1:100 000, NAGRA, Baden,  
 1031 Switzerland, NAGRA Technischer Bericht NTB 84-25, 263 pp., 1984.

1032 Nagra: Zur Tektonik der zentralen Nordschweiz - Interpretation aufgrund regionaler Seismik, Oberflächengeologie  
 1033 und Tiefbohrungen, NAGRA, Wettingen, Switzerland, NAGRA Technischer Bericht NTB 90-04, 277 pp., 1991.

1034 Nagra: 3D-Seismik: Räumliche Erkundung der mesozoischen Sedimentschichten im Zürcher Weinland, NAGRA,  
 1035 Wettingen, Switzerland, NAGRA Technischer Bericht NTB 00-03, 180 pp., 2001.

1036 Nagra: Geologische Entwicklung der Nordschweiz, Neotektonik und Langzeitszenarien Zürcher Weinland,  
 1037 NAGRA, Wettingen, Switzerland, NAGRA Technischer Bericht NTB 99-08, 257 pp., 2002a.

1038 Nagra: Projekt Opalinuston: Synthese der geowissenschaftlichen Untersuchungsergebnisse Entsorgungsnachweis  
 1039 für abgebrannte Brennelemente, verglaste hochaktive sowie langlebige mittelaktive Abfälle, NAGRA, Wettingen,  
 1040 Switzerland, NAGRA Technischer Bericht NTB 02-03, 714 pp., 2002b.

1041 Nagra: Vorschlag geologischer Standortgebiete für das SMA-und das HAA-Lager, NAGRA, Wettingen,  
 1042 Switzerland, NAGRA Technischer Bericht NTB 08-04, 477 pp., 2008.

1043 Nagra: Analyse des rezenten Spannungsfelds der Nordschweiz, NAGRA, Wettingen, Switzerland, NAGRA  
 1044 Arbeitsbericht NAB 12-05, 146 pp., 2013.

1045 Nagra: Tektonische Karte des Nordschweizer Permokarbontrags: Aktualisierung basierend auf 2D-Seismik und  
1046 Schweredaten, NAGRA, Wettingen, Switzerland, NAGRA Arbeitsbericht NAB 14-17, 64 pp., 2014.

1047 Nagra: 3D Seismic Interpretation of Stratigraphic Horizons and Structures in Time Domain, NAGRA, Wettingen,  
1048 Switzerland, NAGRA Arbeitsbericht NAB 23-19, 151 pp., 2024a.

1049 Nagra: Geological Properties of the Jura Ost, Nördlich Lägern and Zürich Nordost Siting Regions for Safety  
1050 Assessment, NAGRA, Wettingen, Switzerland, NAGRA Arbeitsbericht NAB 24-10 Rev. 1, 44 pp., 2024b.

1051 Nagra: Geosynthesis of Northern Switzerland, NAGRA, Wettingen, Switzerland, NAGRA Technischer Bericht  
1052 NTB 24-17, 604 pp., 2024c.

1053 Nagra: In-Situ Stress Field in the Siting Regions Jura Ost, Nördlich Lägern and Zürich Nordost, NAGRA,  
1054 Wettingen, Switzerland, NAGRA Arbeitbericht NAB 24-19, 131 pp., 2024d.

1055 Nicol, A., Walsh, J., Childs, C., and Manzocchi, T.: Chapter 6 - The growth of faults, in: Understanding Faults,  
1056 edited by: Tanner, D., and Brandes, C., Elsevier, 221–255, <https://doi.org/10.1016/B978-0-12-815985-9.00006-0>,  
1057 2020.

1058 Pascal, C. and Gabrielsen, R. H.: Numerical modeling of Cenozoic stress patterns in the mid-Norwegian margin  
1059 and the northern North Sea, *Tectonics*, 20, 585–599, <https://doi.org/10.1029/2001TC900007>, 2001.

1060 Pijnenburg, R. P. J., Verberne, B. A., Hangx, S. J. T., and Spiers, C. J.: Inelastic Deformation of the Slochteren  
1061 Sandstone: Stress-Strain Relations and Implications for Induced Seismicity in the Groningen Gas Field, *Journal*  
1062 *of Geophysical Research: Solid Earth*, 124, 5254–5282, <https://doi.org/10.1029/2019JB017366>, 2019.

1063 Preusser, F., Graf, H. R., Keller, O., Krayss, E., and Schlüchter, C.: Quaternary glaciation history of northern  
1064 Switzerland, *E&G Quaternary Sci. J.*, 60, 21, <https://doi.org/10.3285/eg.60.2-3.06>, 2011.

1065 Qin, X., Zhao, X., Zhang, C., Li, P., Chen, Q., and Wang, J.: Measurement and Assessment of the In-Situ Stress  
1066 of the Shazao yuan Rock Block, a Candidate Site for HLW Disposal in Northwest China, *Rock Mechanics and*  
1067 *Rock Engineering*, 57, 4011–4031, <https://doi.org/10.1007/s00603-024-03775-z>, 2024.

1068 Rajabi, M., Heidbach, O., Tingay, M., and Reiter, K.: Prediction of the present-day stress field in the Australian  
1069 continental crust using 3D geomechanical–numerical models, *Australian Journal of Earth Sciences*, 64, 435–454,  
1070 <https://doi.org/10.1080/08120099.2017.1294109>, 2017a.

1071 Rajabi, M., Tingay, M., and Heidbach, O.: The present-day state of tectonic stress in the Darling Basin, Australia:  
1072 Implications for exploration and production, *Marine and Petroleum Geology*, 77, 776–790,  
1073 <https://doi.org/10.1016/j.marpetgeo.2016.07.021>, 2016.

1074 Rajabi, M., Tingay, M., Heidbach, O., Hillis, R., and Reynolds, S.: The present-day stress field of Australia, *Earth-*  
1075 *Science Reviews*, 168, 165–189, <https://doi.org/10.1016/j.earscirev.2017.04.003>, 2017b.

1076 Rajabi, M., Tingay, M., Heidbach, O., and King, R.: The Role of Faults and Fractures in Local and Regional  
1077 Perturbation of Present-day Horizontal Stresses - An Example from the Clarence-Moreton Basin, Eastern  
1078 Australia, 2015, 1–5, <https://doi.org/10.3997/2214-4609.201413346>, 2015.

1079 Rajabi, M., Tingay, M., King, R., and Heidbach, O.: Present-day stress orientation in the Clarence-Moreton Basin  
1080 of New South Wales, Australia: a new high density dataset reveals local stress rotations, *Basin Research*, 29, 622–  
1081 640, <https://doi.org/10.1111/bre.12175>, 2017c.

1082 Rajabi, M., Ziegler, M., Heidbach, O., Mukherjee, S., and Esterle, J.: Contribution of mine borehole data toward  
1083 high-resolution stress mapping: An example from northern Bowen Basin, Australia, *International Journal of Rock*  
1084 *Mechanics and Mining Sciences*, 173, 105630, <https://doi.org/10.1016/j.ijrmms.2023.105630>, 2024.

1085 Reisdorf, A. G., Wetzel, A., Schlatter, R., and Jordan, P.: The Staffelegg Formation: a new stratigraphic scheme  
1086 for the Early Jurassic of northern Switzerland, *Swiss Journal of Geosciences*, 104, 97–146,  
1087 <https://doi.org/10.1007/s00015-011-0057-1>, 2011.

1088 Reiter, K. and Heidbach, O.: 3-D geomechanical–numerical model of the contemporary crustal stress state in the  
1089 Alberta Basin (Canada), *Solid Earth*, 5, 1123–1149, <https://doi.org/10.5194/se-5-1123-2014>, 2014.

1090 Reiter, K., Heidbach, O., and Ziegler, M. O.: Impact of faults on the remote stress state, *Solid Earth*, 15, 305–327,  
1091 <https://doi.org/10.5194/se-15-305-2024>, 2024.

1092 Richardson, R. M., Solomon, S. C., and Sleep, N. H.: Tectonic stress in the plates, *Reviews of Geophysics*, 17,  
1093 981–1019, <https://doi.org/10.1029/RG017i005p00981>, 1979.

1094 Roberts, D. and Myrvang, A.: Contemporary stress orientation features and horizontal stress in bedrock,  
1095 Trøndelag, central Norway, *NGU Bull.*, 442, 53–63, 2004.

1096 Roche, V., Camanni, G., Childs, C., Manzocchi, T., Walsh, J., Conneally, J., Saqab, M. M., and Delogkos, E.:  
1097 Variability in the three-dimensional geometry of segmented normal fault surfaces, *Earth-Science Reviews*, 216,  
1098 103523, <https://doi.org/10.1016/j.earscirev.2021.103523>, 2021.

1099 Saucier, F., Humphreys, E., and Weldon II, R.: Stress near geometrically complex strike-slip faults: Application  
1100 to the San Andreas Fault at Cajon Pass, southern California, *Journal of Geophysical Research: Solid Earth*, 97,  
1101 5081–5094, <https://doi.org/10.1029/91JB02644>, 1992.

1102 Schmid, S. M., Pfiffner, O. A., Froitzheim, N., Schönborn, G., and Kissling, E.: Geophysical-geological transect  
1103 and tectonic evolution of the Swiss-Italian Alps, *Tectonics*, 15, 1036–1064, <https://doi.org/10.1029/96TC00433>,  
1104 1996.

1105 Schmid, S. M., Pfiffner, O. A., Schönborn, G., Froitzheim, N., and Kissling, E.: Integrated cross section and  
1106 tectonic evolution of the Alps along the Eastern Traverse., in: *Deep Structure of the Alps, Results from NFP 20*,  
1107 edited by: Pfiffner, O. A., Lehner, P., Heitzmann, P., Müller, S., and Steck, A., Birkhäuser Verlag, Birkhäuser,  
1108 Basel, 289–304, 1997.

1109 Schoenball, M., Dorbath, L., Gaucher, E., Wellmann, J. F., and Kohl, T.: Change of stress regime during  
1110 geothermal reservoir stimulation, *Geophysical Research Letters*, 41, 1163–1170,  
1111 <https://doi.org/10.1002/2013GL058514>, 2014.

1112 Seithel, R., Gaucher, E., Mueller, B., Steiner, U., and Kohl, T.: Probability of fault reactivation in the Bavarian  
1113 Molasse Basin, *Geothermics*, 82, 81–90, <https://doi.org/10.1016/j.geothermics.2019.06.004>, 2019.

1114 Sibson, R., Ghisetti, F., and Ristau, J.: Stress Control of an Evolving Strike-Slip Fault System during the 2010–  
1115 2011 Canterbury, New Zealand, Earthquake Sequence, *Seismological Research Letters*, 82, 824–832,  
1116 <https://doi.org/10.1785/gssrl.82.6.824>, 2011.

1117 Sibson, R. H.: Implications of fault-valve behaviour for rupture nucleation and recurrence, *Tectonophysics*, 211,  
1118 283–293, [https://doi.org/10.1016/0040-1951\(92\)90065-E](https://doi.org/10.1016/0040-1951(92)90065-E), 1992.

1119 Sinclair, H. D. and Allen, P. A.: Vertical versus horizontal motions in the Alpine orogenic wedge: stratigraphic  
1120 response in the foreland basin, *Basin Research*, 4, 215–232, <https://doi.org/10.1111/i.1365-2117.1992.tb00046.x>,  
1121 1992.

1122 Smart, K. J., Ferrill, D. A., Morris, A. P., and McGinnis, R. N.: Geomechanical modeling of stress and strain  
1123 evolution during contractional fault-related folding, *Tectonophysics*, 576–577, 171–196,  
1124 <https://doi.org/10.1016/j.tecto.2012.05.024>, 2012.

1125 Sommaruga, A., Eichenberger, U., and Marillier, F.: Seismic Atlas of the Swiss Molasse Basin, *Matériaux pour la  
1126 Géologie de la Suisse – Géophysique*, 2012.

1127 Stromeyer, D., Heidbach, O., and Ziegler, M.: Tecplot 360 Add-on GeoStress v. 2.0. V. 2.0, GFZ Data Services  
1128 [code], <https://doi.org/10.5880/wsm.2020.001>, 2020.

1129 Su, S. and Stephansson, O.: Effect of a fault on in situ stresses studied by the distinct element method, *International  
1130 Journal of Rock Mechanics and Mining Sciences*, 36, 1051–1056, [https://doi.org/10.1016/S1365-1609\(99\)00119-2](https://doi.org/10.1016/S1365-1609(99)00119-2), 1999.

1132 Tanner, D. C. and Brandes, C.: Chapter 1 - Introduction, in: Understanding Faults, edited by: Tanner, D., and  
1133 Brandes, C., Elsevier, 1–10, <https://doi.org/10.1016/B978-0-12-815985-9.00001-1>, 2020.

1134 Tavener, E., Flottmann, T., and Brooke-Barnett, S.: In situ stress distribution and mechanical stratigraphy in the  
1135 Bowen and Surat basins, Queensland, Australia, Geological Society, London, Special Publications, 458, 31–47,  
1136 doi:10.1144/SP458.4, 2017.

1137 Tingay, M. R. P., Hillis, R. R., Morley, C. K., King, R. C., Swarbrick, R. E., and Damit, A. R.: Present-day stress  
1138 and neotectonics of Brunei: Implications for petroleum exploration and production, AAPG Bulletin, 93, 75–100,  
1139 <https://doi.org/10.1306/08080808031>, 2009.

1140 Treffeisen, T. and Henk, A.: Representation of faults in reservoir-scale geomechanical finite element models – A  
1141 comparison of different modelling approaches, Journal of Structural Geology, 131, 103931,  
1142 <https://doi.org/10.1016/j.jsg.2019.103931>, 2020.

1143 Vadacca, L., Rossi, D., Scotti, A., and Buttinelli, M.: Slip Tendency Analysis, Fault Reactivation Potential and  
1144 Induced Seismicity in the Val d'Agri Oilfield (Italy), Journal of Geophysical Research: Solid Earth, 126,  
1145 2019JB019185, <https://doi.org/10.1029/2019JB019185>, 2021.

1146 Viganò, A., Ranalli, G., Andreis, D., and Martin, S.: Inversion for the static friction coefficient of seismogenic  
1147 faults: Application to induced seismicity of the Basel Enhanced Geothermal System, Switzerland, Journal of  
1148 Geodynamics, 145, 101843, <https://doi.org/10.1016/j.jog.2021.101843>, 2021.

1149 Yale, D. P.: Fault and stress magnitude controls on variations in the orientation of in situ stress, in: Fracture and  
1150 In-Situ Stress Characterization of Hydrocarbon Reservoirs, edited by: Ameen, M., Geological Society of London,  
1151 0, <https://doi.org/10.1144/GSL.SP.2003.209.01.06>, 2003.

1152 Yale, D. P., Rodriguez, J. M., Mercer, T. B., and Blaisdell, D. W.: In-situ Stress Orientation and the Effects of  
1153 Local Structure – Scott Field, North Sea, Rock Mechanics in Petroleum Engineering, Delft, Netherlands, 29–31  
1154 Aug, <https://doi.org/10.2118/28146-MS>, 1994.

1155 Yale, D. P. and Ryan, T. C.: In-Situ Stress and Hydraulic Fracture Orientation in the Mid-Continent Area, US, 1st  
1156 North American Rock Mechanics Symposium, Austin, Texas, 1–3 June, 1994.

1157 Yale, D. P., Strubhar, M. K., and El Rabaa, A. W.: Determination of Hydraulic Fracture Direction, San Juan Basin,  
1158 New Mexico, SPE Production Operations Symposium, Oklahoma City, Oklahoma 21–23 March,  
1159 <https://doi.org/10.2118/25466-MS>, 1993.

1160 Yan, H., Bakk, A., Holt, R. M., and Lozovskyi, S.: Numerical analysis of stress path evolution in the overburden of  
1161 depleting reservoirs: a parametric study, Geomechanics and Geophysics for Geo-Energy and Geo-Resources, 11,  
1162 91, 10.1007/s40948-025-00989-5, 2025.

1163 Zakhарова, Н. В. and Goldberg, D. S.: In situ stress analysis in the northern Newark Basin: Implications for  
1164 induced seismicity from CO<sub>2</sub> injection, Journal of Geophysical Research: Solid Earth, 119, 2362–2374,  
1165 <https://doi.org/10.1002/2013JB010492>, 2014.

1166 Zang, A. and Stephansson, O.: Stress field of the earth's crust, 2010, Springer Dordrecht, New York, NY, 324 pp.,  
1167 <https://doi.org/10.1007/978-1-4020-8444-7>, 2010.

1168 Ziegler, M. O. and Heidbach, O.: The 3D stress state from geomechanical-numerical modelling and its  
1169 uncertainties: a case study in the Bavarian Molasse Basin, Geothermal Energy, 8, 11,  
1170 <https://doi.org/10.1186/s40517-020-00162-z>, 2020.

1171 Ziegler, M. O. and Heidbach, O.: Python Script PyFAST Calibration v.1.0 V. 1.0, GFZ Data Services [code],  
1172 <https://doi.org/10.5880/wsm.2021.003>, 2021.

1173 Ziegler, M. O., Heidbach, O., Reinecker, J., Przybycin, A. M., and Scheck-Wenderoth, M.: A multi-stage 3-D  
1174 stress field modelling approach exemplified in the Bavarian Molasse Basin, Solid Earth, 7, 1365–1382,  
1175 <https://doi.org/10.5194/se-7-1365-2016>, 2016.

1176 Ziegler, M. O., Seithel, R., Niederhuber, T., Heidbach, O., Kohl, T., Müller, B., Rajabi, M., Reiter, K., and Röckel,  
1177 L.: Stress state at faults: the influence of rock stiffness contrast, stress orientation, and ratio, *Solid Earth*, 15, 1047–  
1178 1063, <https://doi.org/10.5194/se-15-1047-2024>, 2024.

1179 Ziegler, M. O., Ziebarth, M., and Reiter, K.: Python Script Apple PY v1.3. V. 1.3,  
1180 <https://doi.org/10.5880/wsm.2020.002>, 2020.

1181 Zoback, M. and Healy, J.: Friction, faulting and in situ stress, *Annales geophysicae* (1983), 2, 689–698, 1984.

1182 Zoback, M., Hickman, S., Ellsworth, W., and the, S. S. T.: Scientific Drilling Into the San Andreas Fault Zone -  
1183 An Overview of SAFOD's First Five Years, *Sci. Dril.*, 11, 14–28, <https://doi.org/10.2204/iodp.sd.11.02.2011>,  
1184 2011.

1185 Zoback, M. D.: *Reservoir Geomechanics*, Cambridge University Press, Cambridge,  
1186 <https://doi.org/10.1017/CBO9780511586477>, 2009.

1187 Zoback, M. D., Zoback, M. L., Mount, V. S., Suppe, J., Eaton, J. P., Healy, J. H., Oppenheimer, D., Reasenberg,  
1188 P., Jones, L., Raleigh, C. B., Wong, I. G., Scotti, O., and Wentworth, C.: New Evidence on the State of Stress of  
1189 the San Andreas Fault System, *Science*, 238, 1105–1111, <https://doi.org/10.1126/science.238.4830.1105>, 1987.

1190 Zoback, M. L.: First- and second-order patterns of stress in the lithosphere: The World Stress Map Project, *Journal*  
1191 *of Geophysical Research: Solid Earth*, 97, 11703–11728, <https://doi.org/10.1029/92JB00132>, 1992.

1192 Zoback, M. L., Zoback, M. D., Adams, J., Assumpção, M., Bell, S., Bergman, E. A., Blümling, P., Brereton, N.  
1193 R., Denham, D., Ding, J., Fuchs, K., Gay, N., Gregersen, S., Gupta, H. K., Gvishiani, A., Jacob, K., Klein, R.,  
1194 Knoll, P., Magee, M., Mercier, J. L., Müller, B. C., Paquin, C., Rajendran, K., Stephansson, O., Suarez, G., Suter,  
1195 M., Udiás, A., Xu, Z. H., and Zhizhin, M.: Global patterns of tectonic stress, *Nature*, 341, 291–298,  
1196 <https://doi.org/10.1038/341291a0>, 1989.

1197